Tin whiskers: experiments and modelling

Hektor, Johan

2018

Document Version:
Publisher's PDF, also known as Version of record

Preface

This thesis is the result of my doctoral studies at the Division of Solid Mechanics, Lund University. First and foremost I would like to express my gratitude to my supervisors Matti Ristinmaa and Stephen Hall for their support and for sharing their vast knowledge with me during the past six years. A special thanks to Matti for letting me focus on experimental work, even though that was not at all the plan from the start. I would also like to thank Srinivasan Iyengar and Håkan Hallberg for their supervision at the beginning of my studies, and Håkan also for convincing me to start as a PhD student in the first place. My colleagues in France Jean-Sébastien Micha, Odile Robach, Jean-Baptiste Marijon, Jon Wright, and Olivier Castelnau all deserve thanks for making my short stays in Paris and Grenoble so enjoyable.

I must also thank all my past and current colleagues at the Division of Solid Mechanics for making my time here such a great experience. Sara, Jonas, and Stefanos all deserve a big thanks for all the fun times at and (mostly) out of the office. Thank you also to the 'Falafel, Babylon, Beers' gang for filling most Wednesday nights with just that. Of course, I am also grateful to my family for their unrivalled support. Finally and most importantly, I thank my beloved Kim for everything she has done for me; I am truly happy to have her in my life.

Lund, November 2018
Johan Hektor

Abstract

Tin whiskers are hair-like single crystals that spontaneously grow from tin-coated surfaces. Whiskers are commonly found in electronic components, where tin coatings are used in, e.g., soldering applications, and to protect components from corrosion. Whiskers are known to cause short-circuits leading to failure of electronic components. The exact mechanisms responsible for whisker formation and growth are not fully understood. It is, however, believed that whiskers grow as a way to relax stress in the tin coating and that compressive stress gradients drive the growth. The stress in the coating is mainly caused by the formation and growth of the intermetallic compound Cu_6Sn_5 in the interface region between the copper substrate and the tin layer.

This thesis presents numerical simulations and experimental investigations related to the growth and formation of tin whiskers on tin coated copper substrates. The aim of the experimental work has been to verify the existence of a compressive stress gradient and to characterise the microstructure around tin whiskers in 2D as well as 3D. This was realised using different x-ray diffraction methods, namely scanning Laue microdiffraction, differential aperture x-ray microscopy (DAXM), and scanning 3D x-ray diffraction (3DXRD). Laue microdiffraction was used to study the evolution of the microstructure around two whiskers over a period ranging from 4 to 21 months of ageing. The hydrostatic stress field in the tin coating was estimated by assuming plane stress conditions. It was found that the stress field was highly inhomogeneous. It was possible to identify ridges of high compressive stress leading to the whisker. These ridges, which have not been observed previously, are potentially driving diffusion of tin from specific regions of the coating towards the root of the whisker.

DAXM and 3DXRD were used to study the microstructure around a whisker in three dimensions. Using DAXM, through-depth variations of the deviatoric strain field were measured for the first time. Deep in the coating, where the Cu_6Sn_5 is present, the deviatoric strain was high. This indicates that the growth of the intermetallic phase causes plastic deformation of the tin coating. A novel scanning 3DXRD tomography technique was used to map out intragranular variations in the unit cell parameters and the grain orientations with sub-micrometre resolution. A short (4 µm) radial gradient in hydrostatic stress was observed around the root of the whisker. This gradient together with long-range diffusion from specific regions could provide the driving force for whisker growth. From the 3DXRD data, it was also possible to determine the location of Cu_6Sn_5 in the sample. A large grain of Cu_6Sn_5 was found right below the whisker which seems to have caused distortion of the nearby tin grains. We also studied the evolution of the microstructure during heat treatment. The heat treatment encouraged the formation of the intermetallic phase and also led to coarsening of the tin grains.

The numerical simulations in this thesis are based on a multiphase field model. This model is one of few phase field models existing that includes diffusion as well as elastic and plastic deformation. The model was used to study the growth of Cu_6Sn_5 during room temperature ageing, specifically the effect of the curvature of the intermetallic layer on the stress and plastic deformation of the tin coating was investigated. It was found that a high curvature led to localisation of plastic deformation in the region above the highly curved grain.

Sammanfattning

Så kallade tenn-whiskers kan orsaka stor skada genom att kortsluta elektronikkomponenter. Ett flertal spektakulära fall av whisker-relaterade kortslutningar finns rapporterade, bland annat har kontrollsystem i åtminstone tre satelliter kortslutits på grund av whiskers. Whiskers är mikroskopiska trådar som spontant växer ut från ytor belagda med tenn. Trådarna är några mikrometer breda, några hundradelar av bredden av ett hårstrå, men kan bli flera millimeter långa. Lösningen på problemet med kortslutningar orsakade av whiskers var länge att använda en legering av tenn och bly, istället för rent tenn, i till exempel lödningar eller ytbeläggningar. Av miljöskäl är denna lösning inte längre tillgänglig. Eftersom elektronikkomponenter tenderar att bli mindre och mindre ligger det nära till hands att anta att problemen med whiskers kommer öka i framtiden. Detta eftersom även korta whiskers kan orsaka kortslutningar i små komponenter. Mycket resurser läggs därför på att förstå mekanismerna bakom whiskers bildning och tillväxt för att på sikt kunna hitta en alternativ lösning på problemen med kortslutningar.

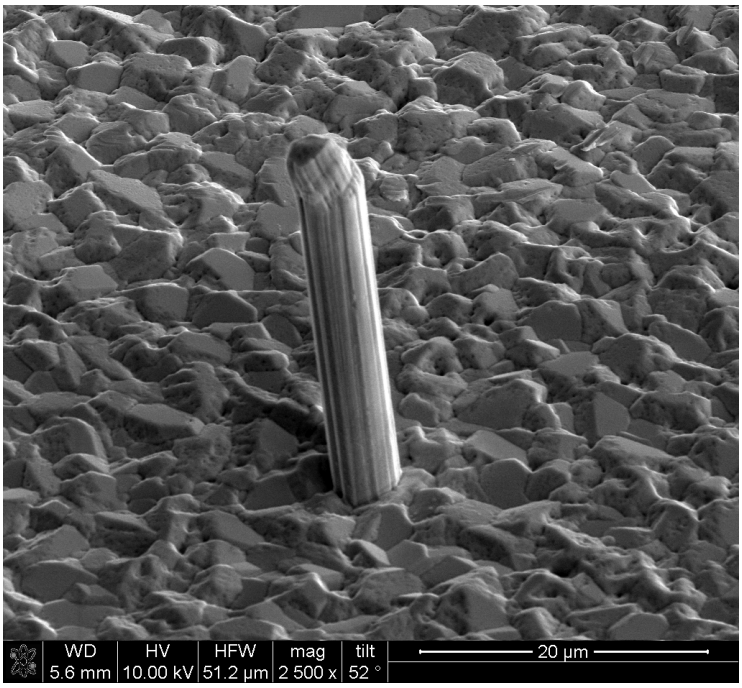

Mikroskopbild av en tennwhisker som växer från ett kopparsubstrat belagt med ett tunt lager av tenn.

Avhandlingen analyserar uppkomst och tillväxt av tennwhiskers, med hjälp av numeriska simuleringar och experimentella mätningar. Med hjälp av röntgenstrålning har enskilda tennwhiskers och den omgivande mikrostrukturen kunnat studeras, både på ytan och i tre dimensioner. Resultat från mätningarna indikerar att den spänningsgradient som tros vara den viktigaste anledningen till att whiskers växer existerar. Den verkar dock vara betydligt mer koncentrerad till vissa områden runt whiskern än vad man tidigare trott. Mätningarna tyder också på att whiskers bildas i korngränser där spänningsgradienten är stor och att de växer för att minska tryckspänningar i de omgivande kornen. Tryckspänningar i tennbeläggningar på kopparsubstrat uppkommer på grund av en fasomvandling

där koppar och tenn tillsammans bildar fasen Cu_6Sn_5.

En numerisk modell för att simulera tillväxten av Cu_6Sn_5 har utvecklats, modellen inkluderar såväl kemiska som mekaniska drivkrafter för tillväxt av Cu_6Sn_5. Den framtagna modellen är en av få fasfältsmodeller som inkluderar diffusion tillsammans med elastisk och plastisk deformation. Resultaten från simuleringarna visar att tillväxten av Cu_6Sn_5 leder till plastisk deformation av tennkornen, nivån och distributionen av plasticitet påverkas av kurvaturen på Cu_6Sn_5-kornen.

Forskningen presenterad i denna avhandling kan leda till ökad kunskap om orsakerna bakom whisker-tillväxt. Sådan kunskap är nödvändig för att hitta en lösning på de problem som whiskers kan ge upphov till. De experimentella metoderna och den utvecklade numeriska modellen kan dessutom användas för att studera många andra fenomen på den mikroskopiska längdskalan.

List of appended papers

This doctoral thesis is based on the following manuscripts:

Paper A
Johan Hektor, Matti Ristinmaa, Håkan Hallberg, Stephen A. Hall, and Srinivasan Iyengar
Coupled diffusion-deformation multiphase field model for elastoplastic materials applied to the growth of Cu_6Sn_5
Acta Materialia 108 (2016), 98-109

Paper B
Johan Hektor, Jean-Sébastien Micha, Stephen A. Hall, Srinivasan Iyengar, and Matti Ristinmaa
Long term evolution of microstructure and stress around tin whiskers investigated using Laue microdiffraction
Submitted for publication

Paper C
Johan Hektor, Jean-Baptiste Marijon, Matti Ristinmaa, Stephen A. Hall, Håkan Hallberg, Srinivasan Iyengar, Jean-Sébastien Micha, Odile Robach, Fanny Grennerat, and Olivier Castelnau
Evidence of 3D strain gradients associated with tin whisker growth
Scripta Materialia 144 (2018), 1-4

Paper D
Johan Hektor, Stephen A. Hall, N. Axel Henningsson, Jonas Engqvist, Matti Ristinmaa, Filip Lenrick, and Jonathan P. Wright
Scanning 3DXRD measurement of grain growth, stress, and formation of Cu_6Sn_5 around a tin whisker during heat treatment
To be submitted for publication

Own Contribution
The author of this thesis has taken the main responsibility for the preparation and writing of all appended papers. The numerical model in Paper A have been developed in collaboration with the co-authors and implemented by the main author. The experiments and analysis of the data in Papers B, C, and D were carried out by the author in collaboration with the co-authors.

Contents

1 Introduction

Coatings of tin (Sn) are often used to protect electronic components from corrosion. Due to the low melting point of 232 °C, tin is also commonly used in solders, both in its pure form and alloyed with, e.g., copper, silver, or lead. In 2006 the European Union enacted the Restriction of Hazardous Substances (RoHS) act which restricted the use of lead in consumer electronics due to its toxicity (European Parliament, 2003). More recently, similar legislation was introduced in other countries such as China, Japan, South Korea and the United States (Cheng et al., 2017). Banning lead caused a renewed interest in the old problem of tin whiskers. Whiskers growing on electronic components can cause electrical short circuits by bridging the gap between two adjacent parts of an electrical component. The maximum current a whisker can carry is at least 32 mA (Dunn, 1976), which is enough to cause permanent short circuits in some cases. Short circuits by whiskers growing in a vacuum, e.g., in space applications, can cause the whisker to form a plasma that can carry hundreds of amperes of current (Brusse et al., 2002). Such events have caused failure of several commercial satellites. In addition to the satellites already mentioned, whisker-related failures in for example nuclear power plants, pacemakers, and missiles have been reported (NASA, 2009).

Tin whiskers are hairlike grains that grow spontaneously from tin coated surfaces. Whiskers are usually found growing from thin films deposited on a substrate material, such as a protective tin coating deposited on a copper electronic component. Typically whiskers are up to a few micrometers wide (Oudat et al., 2018) and 10 to 80 µm long (Fang et al., 2006). In exceptional cases, whiskers can grow to lengths of several millimetres. Figure 1 show scanning electron microscope (SEM) images of two whiskers growing from tin coatings deposited on copper substrates. The two whiskers show very different growth morphologies; one is almost entirely straight with only a slight curvature near the top, the other one has several sharp kinks. The kinks are caused either by a change in how the material is supplied to the whisker root or by rotation and migration of grain boundaries at the base of the whisker (Susan et al., 2013). Whiskers can also form as low aspect ratio surface eruptions, so-called hillocks. Whiskers are formed instead of hillocks when the grain boundaries in the tin coating are pinned, e.g. by grain boundary precipitates of intermetallic compounds (IMC), thus hindering lateral growth of the grain (Boettinger et al., 2005).

The exact mechanisms behind whisker formation are still elusive. During recent years, however, it has been agreed upon that whisker formation is related to stresses in the tin coating and that whiskers grow to relax these stresses (Hektor et al., 2018; Sobiech et al., 2009, 2008; Choi et al., 2003; Sarobol et al., 2013a,b; Pei et al., 2016; Buchovecky et al., 2009; Boettinger et al., 2005; Smetana, 2007). The primary source of stresses in tin coatings on copper substrates is the growth of the intermetallic compound Cu_6Sn_5 that takes place in the interface between the coating and the substrate, as well as in grain boundaries within the coating. The IMC will continue to grow over a long period of time and will therefore continuously regenerate stresses in the coating. Externally applied stresses can also lead to whisker growth, these sources of stress are in general not regenerative and therefore not as critical as the IMC formation. It is believed that the stress gradient from the compressed region close to the IMC to the stress-free whisker drives diffusion of Sn atoms towards the whisker root (Sobiech et al., 2009), making it grow by addition of material at its base (Koonce and Arnold, 1953).

The first observation of tin whiskers was reported in 1951 (Compton et al., 1951). Before that, during the Second World War, cadmium plated capacitors in military equipment was short-circuiting

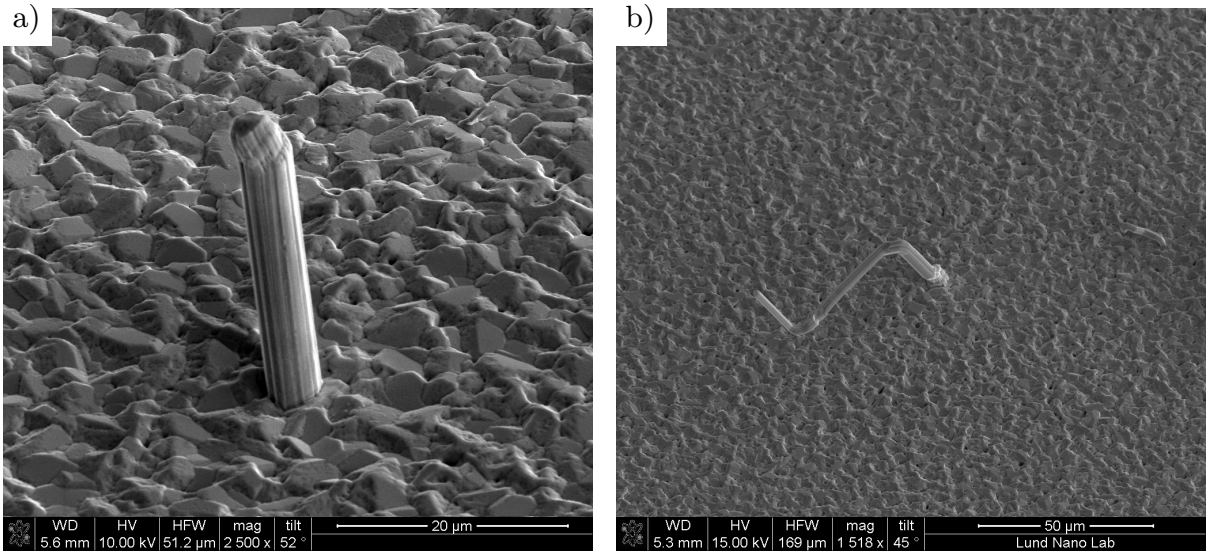

Figure 1: Scanning electron microscope images of tin whiskers with different morphologies. a): A relatively short and straight whisker. b): A long whisker with several kinks.

due to whisker growth (Galyon, 2005; Cobb, 1946). Other metals – such as zinc (Lindborg, 1975), silver (Ohachi and Taniguchi, 1974), and gold (Teverovsky, 2003) – can also grow whiskers. Relatively soon after the first observation of tin whiskers, it was found that alloying tin with lead significantly decreases the risk of whiskers (Pitt and Henning, 1964; Galyon, 2005). For the reason mentioned above, using tin-lead alloys instead of pure tin is no longer a viable solution to the problem of tin whiskers. Further research on when, where, and why tin whiskers form and how to prevent them is therefore much needed. The need for an increased understanding of the mechanisms responsible for whisker growth is also spurred by the current trend of miniaturisation, i.e. making electronic components increasingly smaller. This can potentially lead to significant problems even with short whiskers.

The experimental part of the work presented in this thesis is primarily aimed at characterisation of the stress/strain field around a tin whisker in 3D using x-ray diffraction techniques. In addition, the evolution of the stress field during long-term ageing of a whisker was characterised. By scanning a large area around the whisker, the very early stages of growth of a different whisker was also captured. The modelling endeavour aims at developing a model for the growth of Cu_6Sn_5 including all of the relevant physics leading to whisker formation.

2 The crystal structure of tin

Atoms in metals are arranged in a periodic structure called a crystal lattice, the smallest repeating unit in the crystal lattice is called the unit cell. The behaviour of crystalline materials is, to a large extent, determined by how the atoms in the material are arranged. Depending on temperature tin can exist in two different forms, with different atomic arrangements. At temperatures below 13.2 °C,

Table 1: Lattice parameters for β-tin (Deshpande and Sirdeshmukh, 1961).

Lengths (Å)			Angles (°)		
a	b	c	α	β	γ
5.8318	5.8318	3.1819	90	90	90

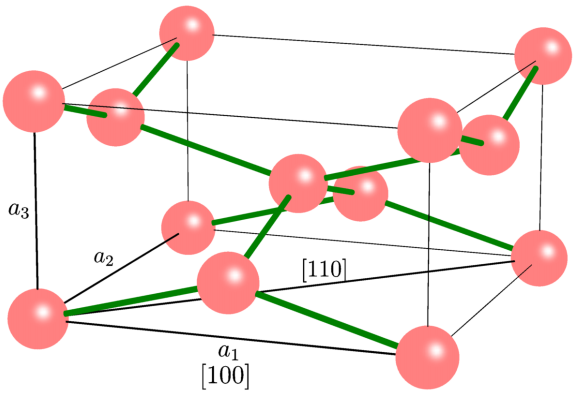

Figure 2: Illustration of the body-centred tetragonal unit cell of tin. The red spheres represent atoms. The green lines show the bonds between atoms. $\boldsymbol{a}_i$ denotes the lattice vectors describing the size and orientation of the unit cell. The Miller indices $[1\,0\,0]$ and $[1\,1\,0]$ indicates the main orientation of the studied tin coatings.

the so-called α-tin, or grey tin, is stable. In this phase, the unit cell is cubic. The α phase have inferior structural properties; tin components transforming to α-tin, due to a decrease in temperature, readily crumbles into a powder – this phenomenon is known as *tin pest* (Cornelius et al., 2017).

At temperatures higher than 13.2 °C, β-tin, or white tin, is the stable phase. In the remainder of this thesis, the word tin is referring to β-tin. An illustration of the unit cell of β-tin is shown in Figure 2. This type of unit cell is called *body-centred tetragonal* (BCT) and is characterised by the fact that one of the crystal axes has a different length than the other two. The orientation and size of the unit cell can be described by three lattice vectors $\boldsymbol{a}_1$, $\boldsymbol{a}_2$, and $\boldsymbol{a}_3$. The lengths of, and angles between, these vectors are called the lattice parameters of the material and are denoted $[a, b, c, \alpha, \beta, \gamma]$. The lattice parameters for β-tin are given in Table 1. Directions, and planes, within the unit cell can be described using Miller indices, $[h\,k\,l]$, such that $[1\,0\,0]$, $[0\,1\,0]$, and $[0\,0\,1]$ lies along the vectors $\boldsymbol{a}_1$, $\boldsymbol{a}_2$, and $\boldsymbol{a}_3$, respectively. In addition to the eight corner atoms and one centre atom typical of BCT unit cells, tin has four extra atoms located at the $\langle 2\,0\,4 \rangle$ positions (Yang and Li, 2006). The low symmetry of this unit cell makes the material properties highly anisotropic. As an example, the coefficient of thermal expansion in the c-direction is twice as large as in the a- and b-directions (Subramanian and Lee, 2006).

Plastic deformation of crystals occurs on specific slip systems with the unit cell. Each slip system is characterised by a slip plane and a slip direction. For the BCT unit cell, there are 32 slip systems,

Table 2: Slip systems for β-tin (Fujiwara and Hirokawa, 1987; Zhou et al., 2009).

Slip plane	Slip direction	Number of slip systems in family
$\{1\,0\,0\}$	$\langle 0\,0\,1\rangle$	2
$\{1\,1\,0\}$	$\langle 0\,0\,1\rangle$	2
$\{1\,0\,0\}$	$\langle 0\,1\,0\rangle$	2
$\{1\,1\,0\}$	$\langle 1\,\bar{1}\,1\rangle$	4
$\{1\,1\,0\}$	$\langle 1\,\bar{1}\,0\rangle$	2
$\{1\,0\,0\}$	$\langle 0\,1\,1\rangle$	4
$\{0\,0\,1\}$	$\langle 0\,1\,0\rangle$	2
$\{0\,0\,1\}$	$\langle 1\,1\,0\rangle$	2
$\{0\,1\,1\}$	$\langle 0\,\bar{1}\,1\rangle$	4
$\{2\,1\,1\}$	$\langle 0\,\bar{1}\,1\rangle$	8

which can be divided into 10 families of symmetrically equivalent slip systems. The slip planes and slip directions for these families are given in Table 2. These slip systems are a key component in the crystal plasticity model outlined in Section 3.2.

3 Modelling of intermetallic compounds in the Cu−Sn system

Phase field modelling is one of the most potent tools in computational materials science. It can be used to simulate the microstructural evolution during a wide range of processes and for a wide variety of materials. Some examples of processes modelled using phase field models include solidification (Boettinger et al., 2002), dendritic growth (Karma and Rappel, 1998), recrystallisation (Takaki et al., 2009), and martensitic phase transformation (Artemev et al., 2001).

This section outlines a phase field model which has been used in Paper A to simulate the growth of the intermetallic compound Cu_6Sn_5 during room temperature ageing. An improved model based on crystal plasticity is also presented, together with some preliminary results.

3.1 Multiphase field modelling

Multiphase field models rely on the representation of a polycrystalline microstructure by a set of non-conserved order parameters which all are continuous functions of space, $\boldsymbol{X}$, and time, t:

$$\boldsymbol{\phi} = (\phi_1(\boldsymbol{X}, t), \phi_2(\boldsymbol{X}, t), \ldots, \phi_n(\boldsymbol{X}, t)) \tag{1}$$

In the simplest models each of the order parameters represent one grain in the microstructure. Within the bulk of grain k, the order parameters take the values

$$\phi_i = \begin{cases} 1, & \text{if } i = k \\ 0, & \text{if } i \neq k \end{cases}. \tag{2}$$

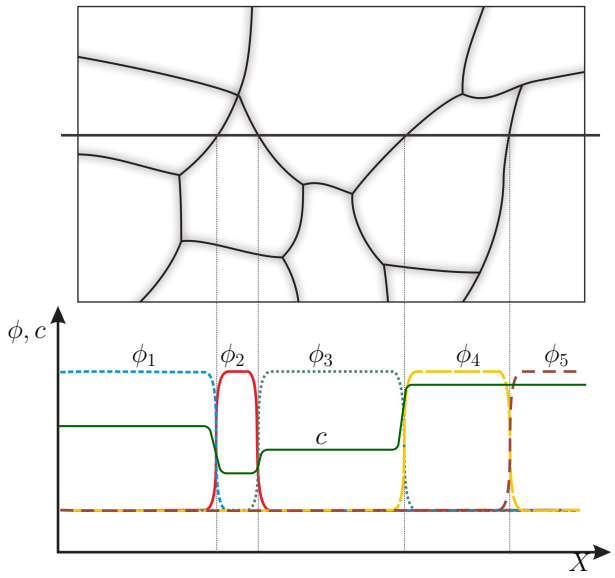

Figure 3: Illustration of how to describe a polycrystalline microstructure using multiple order parameters, ϕ, and a concentration field, c. Figure adapted from Wikipedia contributors (2018).

Consequently, grain boundaries are taken as the regions where two or more order parameters vary smoothly between 0 and 1. This variation occurs over some distance, δ, creating a diffuse interface region. An illustration of how a polycrystalline microstructure can be represented by order parameters is shown in Figure 3. The five grains along the thick black line in the top figure are represented by five order parameters as shown in the bottom figure.

One consequence of the diffuse interfaces is that the position of an interface is implicitly given by a contour of constant values of the order parameter fields (e.g., the grain boundary between grain i and grain j can be taken at $\phi_i = \phi_j = 0.5$). Since no special treatment of grain boundaries are needed, phase field models can be used to simulate microstructures with complex grain morphologies (Moelans et al., 2008). The price to pay for this flexibility is increased computational time and complexity of the simulation. One way to speed up multiphase field simulations is to let the same order parameter represent several grains. This can be done as long as these grains are not in contact with each other by using some form of grain tracking algorithm (Permann et al., 2016). For models containing many grains, this can reduce the computational complexity of the simulation. For simplicity, and due to the low number of grains in the simulations presented in this thesis, no grain tracking algorithm has been used.

Diffusion can be incorporated into multiphase field models in several ways. The route taken in this work follows the so-called Kim-Kim-Suzuki (KKS) model (Kim et al., 1999). In KKS models, conserved field variables $\boldsymbol{x} = (x_1(\boldsymbol{X}, t), x_2(\boldsymbol{X}, t), \dots x_n(\boldsymbol{X}, t))$ representing the molar fraction of a certain chemical species in each phase are used. The molar fraction fields are related to the global molar concentration field, c, through the conservation of mass

$$c(\boldsymbol{X}, t) = \sum_i^n h_i \frac{x_i(\boldsymbol{X}, t)}{V^m}, \tag{3}$$

where

$$h_i = \frac{\phi_i^2}{\sum_j^n \phi_j^2} \tag{4}$$

is an interpolation function used to determine properties of the interface regions (Moelans, 2011) and V^m is the molar volume which is assumed to be the same for all phases.

The equations governing the evolution of the concentration field and the order parameter fields can be derived in a thermodynamically consistent way using the constitutive framework presented in Ammar et al. (2009). The extension of this framework to a multiphase field setting is one of the key results of Paper A. It is shown that the evolution equations for c and ϕ_i are

$$\dot{c} = \boldsymbol{\nabla} \cdot M(\boldsymbol{\phi}) \boldsymbol{\nabla} \frac{\partial f}{\partial c} \tag{5}$$

and

$$\dot{\phi}_i = L(\boldsymbol{\phi}) \left(\boldsymbol{\nabla} \cdot \alpha \boldsymbol{\nabla} \phi_i - \frac{\partial f}{\partial \phi_i} \right), \tag{6}$$

respectively. The mobility terms $M(\boldsymbol{\phi})$ and $L(\boldsymbol{\phi})$ are functions of all order parameters. This makes it possible to have higher mobility in certain grains or phases. Additional physics can be added to the model through the free energy density f. The free energy density in Paper A includes terms for chemical free energy, interface free energy, and mechanical free energy taking elasticity and plasticity into account.

The plastic deformation is modelled using an isotropic von Mises plasticity model. In this type of models, the plastic deformation is determined by the von Mises yield criterion

$$g = \sigma^{eff} - \sigma_0^y - H\kappa(\bar{\rho}) \leq 0, \tag{7}$$

where σ^{eff} is the von Mises stress, σ_0^y is the initial yield stress, κ is an internal variable, and H is a hardening parameter. During elastic deformation $g < 0$, which implies that plastic deformation cannot occur until the von Mises stress equals the initial yield stress. Upon further plastic deformation, the stress and the internal variable are determined so that $g = 0$. The internal variable $\kappa(\bar{\rho})$ is describing the amount of plastic deformation. In this model, κ is taken as a function of the relative density of dislocations $\bar{\rho}$ such that

$$\kappa = \sqrt{\bar{\rho}} - 1. \tag{8}$$

In the initial stage, $\bar{\rho} = 1$. The evolution of the dislocation density is then assumed to follow a Kocks-Mecking law

$$\dot{\bar{\rho}} = \left(d_1 \sqrt{\bar{\rho}} - d_2 \bar{\rho} \right) \dot{\lambda} \tag{9}$$

where d_1 and d_2 are parameters controlling the creation and annihilation of dislocations, respectively. The plastic multiplier $\dot{\lambda}$ in Equation (9) is determined using Equations (7) and (8) so that $g = 0$.

In Paper A the multiphase field model outlined above was used to study the growth of Cu_6Sn_5 during room temperature ageing. The volume change caused by the formation of the IMC is simulated by applying a transformation strain to the IMC that is forming during the simulation, this will cause stresses and plastic deformation to develop in the microstructure. One of the aspects studied was how the initial curvature of the IMC layer affects the build-up of stress in the Sn coating. In

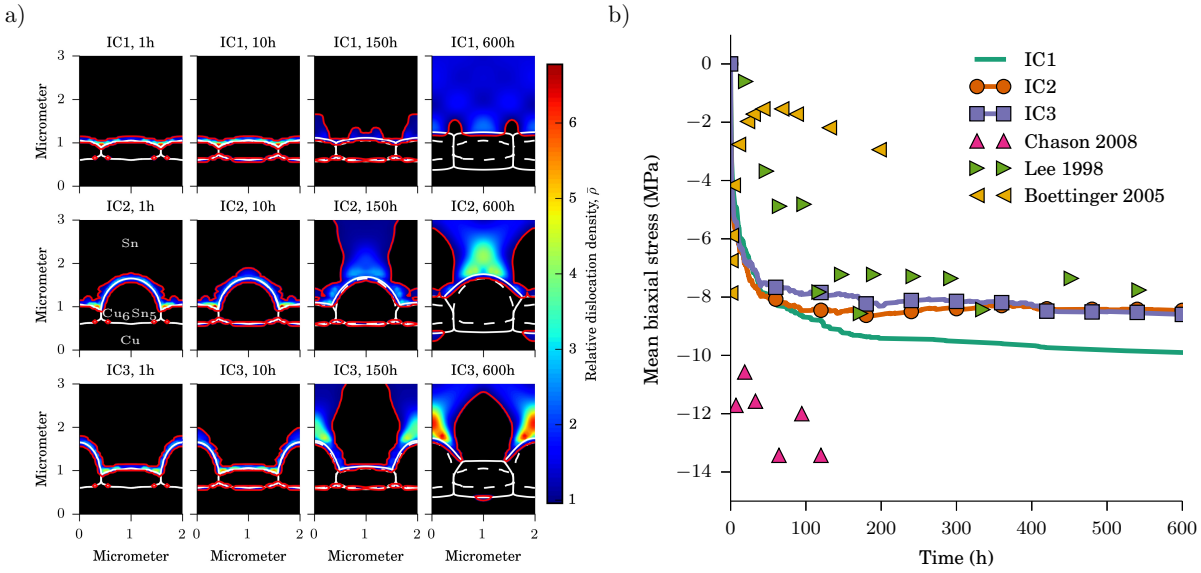

Figure 4: a): Evolution of the microstructure during room temperature ageing for three different initial shapes of the Cu_6Sn_5 layer. The Sn grain is coloured by the relative dislocation density.
b): Mean biaxial stress in the Sn grain as a function of ageing time.

Figure 4a the evolution of the dislocation density, $\bar{\rho}$ is shown for three different curvatures of the IMC layer. A dislocation density larger than 1 indicates that plastic deformation is occurring. It is seen that plastic deformation takes place for all three curvatures, but the dislocation density is significantly higher for the case where the IMC is growing into the grain boundaries of the Sn grains (the boundary conditions of the simulation are set so that the lateral boundaries are representative of grain boundaries). Figure 4b shows the mean biaxial stress in the Sn grain as a function of ageing time. The stress becomes increasingly compressive with time until it flattens out a value of –8 to –10 MPa. This is in excellent agreement with the experimental data presented in Lee and Lee (1998). The trend also agrees with the data in Chason et al. (2008) and Boettinger et al. (2005) even though the level of stress is slightly different.

3.2 Crystal plasticity model

A more accurate description of the mechanical behaviour of the tin coating is obtained by the use of a crystal plasticity model. A crystal plasticity model for metallic materials with a BCT structure is briefly summarised here. The model is based on the multiplicative split of the deformation gradient into an elastic part and a plastic part

$$\boldsymbol{F} = \boldsymbol{F}_i^e \boldsymbol{F}_i^p, \tag{10}$$

where $\boldsymbol{F}_i^e$ and $\boldsymbol{F}_i^p$ denotes the elastic and the plastic deformation gradients for grain i, respectively. For brevity the subscript i is omitted in the following description. In Equation (10) it is assumed that the total deformation gradient, $\boldsymbol{F}$, is the same for all grains co-existing in the same spatial position. This assumption corresponds to the so-called Voigt-Taylor assumption (Hill, 1963). The evolution of

the plastic deformation gradient is given by

$$\dot{\boldsymbol{F}}^p = \left(\sum_{\alpha=1}^{n} \dot{\gamma}^\alpha \boldsymbol{m}^\alpha \otimes \boldsymbol{n}^\alpha \right) \boldsymbol{F}^p \tag{11}$$

where $\dot{\gamma}^\alpha$, $\boldsymbol{m}^\alpha$, and $\boldsymbol{n}^\alpha$ are the slip rate, the slip direction, and the slip plane normal of slip system α. The summation is performed over all 32 slip systems of the BCT crystal; these are given in Table 2. The slip rate for each slip system is calculated as

$$\dot{\gamma}^\alpha = \dot{\gamma}_0^\alpha \left| \frac{\tau^\alpha}{s^\alpha} \right|^{\frac{1}{m}} \operatorname{sgn}\left(\tau^\alpha\right), \tag{12}$$

where $\dot{\gamma}_0^\alpha$ is an initial slip rate and m is the hardening exponent. The resolved shear stress, τ^α, is obtained by projecting the Mandel stress tensor $\boldsymbol{\Sigma}$ – which can be calculated from the deformation gradient and a model for elasticity – onto the slip direction, i.e.:

$$\tau^\alpha = \boldsymbol{m}^\alpha \cdot \boldsymbol{\Sigma} \cdot \boldsymbol{n}^\alpha. \tag{13}$$

Here a linear relationship between the second Piola-Kirchhoff stress tensor in the intermediate configuration, $\boldsymbol{S}$, and the elastic part of the Green-Lagrange strain tensor, $\boldsymbol{E}^e$, is assumed i.e.,

$$\boldsymbol{S} = \mathbb{C} : \boldsymbol{E}^e = \mathbb{C} : \left(\frac{1}{2} \left(\boldsymbol{F}^{eT} \boldsymbol{F}^e - \boldsymbol{I} \right) \right), \tag{14}$$

where $\mathbb{C}$ denotes the elasticity tensor and $\boldsymbol{I}$ is the identity tensor. The Mandel stress is then given by

$$\boldsymbol{\Sigma} = \boldsymbol{F}^{eT} \boldsymbol{F}^e \boldsymbol{S}. \tag{15}$$

Lastly, the slip resistance is taken to evolve as

$$\dot{s}^\alpha = \sum_{\beta}^{n} q^{\alpha\beta} h_0 \left| 1 - \frac{s^\beta}{\tau_{sat}^\beta} \right|^c \operatorname{sgn}\left(1 - \frac{s^\beta}{\tau_{sat}^\beta} \right) \left| \dot{\gamma}^\beta \right|, \tag{16}$$

where $q^{\alpha\beta}$, h_0, c, and τ_{sat}^β are hardening parameters.

The coupling between the plasticity and the phase field model is achieved through the free energy density, as described above. The mechanical part of the free energy density is taken as

$$f_u = \sum_i h_i \left(f_i^e + f_i^p \right). \tag{17}$$

The elastic energy is given by

$$f_i^e = \frac{1}{2} \boldsymbol{S}_i : \boldsymbol{E}_i^e. \tag{18}$$

For the plastic energy the following form is adopted:

$$f_i^p = \frac{1}{2} Q \sum_\alpha \sum_\beta q^{\alpha\beta} s_i^\alpha s_i^\beta, \tag{19}$$

where Q is a material parameter.

To simulate nucleation of IMC, a perturbation is introduced in Equation (6) so that

$$\dot{\phi}_{IMC} = L(\boldsymbol{\phi}) \left(\boldsymbol{\nabla} \cdot \alpha \boldsymbol{\nabla} \phi_i - \frac{\partial f}{\partial \phi_{IMC}} \right) + \zeta(t, \boldsymbol{X}). \tag{20}$$

Following Shen et al. (2007), the perturbation is taken as

$$\zeta(t, \boldsymbol{X}) = \begin{cases} \rho \sqrt{\frac{2 k_B T L}{\lambda^2 \Delta t}} & \text{in grain boundaries} \\ 0 & \text{in bulk} \end{cases}, \tag{21}$$

where ρ is a random number, k_B is the Boltzmann constant, T is temperature, λ is the size of an element in the mesh, and Δt is the size of the time step. The rest of the phase field model remains unchanged. This model has been implemented in the MOOSE framework which allows for massively parallel and fully coupled simulations (Gaston et al., 2009). Material parameters used for the simulations described below are presented in Appendix A.

A simplified microstructure, which resembles a precipitate of Cu_6Sn_5 growing in a tin grain boundary, was used to investigate how the orientation of the tin grains influence the growth of the IMC and the evolution of plastic strains. The microstructure consists of a circular grain of copper, located in a grain boundary between two tin grains of different orientation. During the first second of the simulation, a grain of Cu_6Sn_5 will nucleate in the interface between the copper grain and the tin grains. This grain will continue to grow during the rest of the simulation. The simulation domain was taken as a square, $1 \times 0.5\,\mu m^2$, which was discretised using 200×100 4-node elements. Symmetry boundary conditions were applied to all boundaries. As in Paper A, the stresses are caused by the volume change associated with the formation of Cu_6Sn_5. There is not yet any consensus in the literature regarding how large this volume change is, depending on assumptions related to the chemistry of the phase transformation the resulting volume change varies greatly. If it is assumed that the reaction is $6\,Cu + 5\,Sn \longrightarrow Cu_6Sn_5$, i.e., that the IMC is forming from a rule of mixture combination of Cu and Sn, the relative volume change $\frac{\Delta V}{V_0} = -0.056$ which corresponds to a transformation strain of -0.02. In Boettinger et al. (2005), it is argued that such a large volume change would lead to unphysically high stresses in the IMC. Instead, it is suggested that the transformation strain should be in the range 0 to -0.003 To study the effect of the volume change, two cases where studied; in the first case the transformation strain is taken as -0.003, this value was also used in Paper A. For the second case, the transformation strain is taken as -0.02, which corresponds to the rule of mixture combination.

Figure 5 show the evolution of the microstructure during ageing at 150 °C for 100 s, in the top half of the figure results are shown for the case where the transformation strain is small (-0.003), the lower half show results from a simulation with a large transformation strain (-0.02). The orange, white, and red lines indicate the 5×10^{-4}, 1×10^{-3}, and 5×10^{-3} contours of the accumulated slip, which is defined as

$$\bar{\gamma}(t_n) = \int_{t=t_0}^{t_n} \sum_i \left(h_i(t) \sqrt{\sum_\alpha \dot{\gamma}_i^\alpha(t) \dot{\gamma}_i^\alpha(t)} \right) \, dt, \tag{22}$$

where t_n denotes the current time. The orientations of the tin grains are chosen so that for the blue grain the c-axis is pointing out of the figure, while for the green grain the c-axis is pointing in the horizontal direction.

From Figure 5 it is seen that the yellow IMC grain is growing with time. The growth is faster on the copper side than on the tin side. This can be explained by the faster diffusion coefficient of tin, i.e., tin can diffuse faster to the interface between Cu and Cu_6Sn_5 than copper can diffuse to the interface between Sn and Cu_6Sn_5. Minimisation of the interface energy also drives shrinkage of the circular copper grain. Furthermore, the copper grain is shrinking faster in the simulation with low volume change. This is caused by the contribution from elastic energy. When the volume change is large, large stresses are developing in the microstructure which will increase the elastic energy of the system. Clearly, in the case of the large volume change, it is less energetically favourable for the IMC grain to grow into the copper than in the case of the low volume change. It should be noted that in these simulations the copper grain is assumed to deform elastically, this effect might not be present if plastic deformation of the copper grain were considered. The IMC is also growing faster into the tin grains when the volume change is low. Another difference between the two simulations is seen in the shape of the IMC grain. For the simulation with low volume change, the IMC keeps a ring-like morphology throughout the ageing. This is not the case for the large volume change; instead, the IMC-Sn interface takes a more irregular shape. The shape of the IMC is also slightly different in the two tin grains. This indicates that the morphology of the IMC is affected by the orientation of the tin grain it is growing into. It is also seen that the grain boundary between the tin grains is no longer vertical. Instead, it seems like the green grain has started consuming the blue. Since this anisotropy is not seen for the low volume change, this is likely caused by the amount of plastic deformation in the tin grains.

The evolution of plasticity, visualised by the orange, white, and red contour lines, is different in the two tin grains, in the blue grain the size of the plastic zone is smaller than in the green grain. It is seen that in the early stage of the simulation with low volume change, the plastic deformation is confined to a region close to the IMC, with further ageing the plastic zone expands. Wide bands of plasticity are then forming in the horizontal and the vertical directions of the green grain. These bands extend to the boundaries already after 20 seconds. A similar evolution is seen in the blue grains, the level of plastic slip in the bands is however, significantly lower. The plastic zone keeps growing during further ageing. From this simulation, it can be concluded that, for this type of deformation, the green grain which has the c-axis in the horizontal plane is more prone to plastic deformation. A similar evolution of the plastic slip is seen in the simulation with large volume change, the level of plastic slip is, however, much higher. After 20 s of ageing, the accumulated plastic slip in the both tin grains exceed 1×10^{-3} everywhere and the only region where the plastic slip is lower than 5×10^{-3} is in the lower right corner.

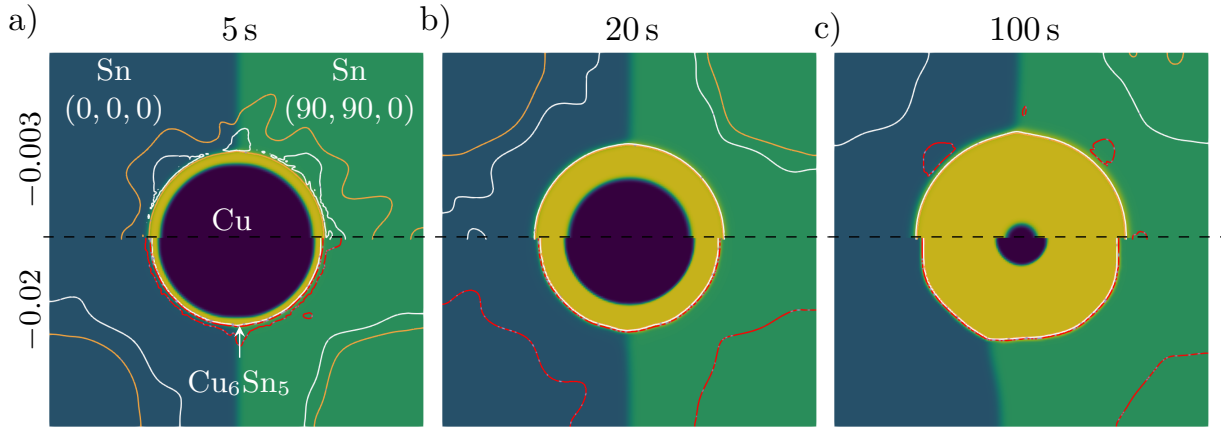

Figure 5: Evolution of the microstructure and the plastic zone during ageing at 150 °C for a): 5 s, b): 20 s, and c): 100 s. The top half of the figure show results for the case where the volume change is -0.003, in the bottom half the volume change was taken as -0.02. The size of the domain is $1 \times 1\,\mu m^2$. The orange, white, and red contour lines indicate regions where the plastic slip is larger than 5×10^{-4}, 1×10^{-3}, and 5×10^{-3}, respectively. The numbers in parenthesis are the Bunge-Euler angles describing the orientation of the tin grains.

4 Characterisation of the microstructure around tin whiskers using x-ray diffraction

The samples studied in the experiments discussed in Section 4.2 consists of high purity copper sheets coated with a thin layer of tin. The coating was deposited using electron-beam physical vapour deposition (Shishkovsky and Lebedev, 2011). This method works by placing the substrate to be coated, together with an ingot of the coating material, in a vacuum chamber. The ingot is then bombarded by electrons from an electron gun. This process cause atoms from the ingot to sputter, i.e., the atoms will be knocked loose by the electron beam. The sputtered atoms are then condensed on the substrate to produce the coating; material will also be deposited on the walls of the vacuum chamber. The deposition process was continued until the tin layer was approximately 7 µm thick, this took about two hours.

After deposition, the samples were aged in ambient conditions to give time for whiskers to grow. Prior to the experiments, suitable whiskers were identified using SEM. The primary selection criterion was that the selected whiskers should be relatively isolated, the idea behind this was that the measured microstructure should only be affected by a single whisker. For the experiments using Laue diffraction, discussed in Sections 4.2.1 and 4.2.2, no further sample preparation was needed. The 3DXRD experiments presented in Section 4.2.3 are more challenging in terms of sample preparation than the Laue experiments. Since 3DXRD is done in transmission mode, i.e., the x-rays penetrate through the sample, a smaller sample is needed. It is also advantageous if the sample has rotational symmetry. The preparation of the sample for the 3DXRD experiment is discussed in the next section.

4.1 Preparation of the 3DXRD sample using focused ion beam milling

Focused ion beam (FIB) instruments have been used to prepare electron transparent specimens for transmission electron microscopy (TEM) since the early 1990s (Giannuzzi and Stevie, 1999). FIB instruments are often combined with an SEM into a dual beam system. This combination makes it possible to use the milling and deposition capabilities of the FIB together with the imaging and measurement capabilities of the SEM within the same instrument. The FIB operates by focusing a beam of ions, typically gallium (Ga), onto the sample. Upon impact, energy is transferred from the ion beam to the solid sample. The energy transfer results in the following interactions between the ions and the atoms in the sample: reflection and backscattering of ions, emission of secondary electrons, electromagnetic radiation, atomic sputtering and ion emission, and damage and heating of the sample (Volkert and Minor, 2007). Depending on the density of the sample, the Ga ions penetrates 5 to 50 nm into the sample before coming to rest (Volkert and Minor, 2007).

The sputtering interaction between the ion beam and the sample means that the FIB can be used to remove material locally. During FIB milling the sputtered atoms may redeposit at some other location of the sample. To protect the sample surface from re-deposition, and other beam-induced damage, the FIB can first be used to deposit protective material on the surface. This is done through chemical vapour deposition (CVD). The precursor gas, containing, e.g., tungsten (W) or platinum (Pt), is sprayed onto the surface, where it adsorbs, using a nozzle. The ion beam will then decompose the gas, leaving a thin film of the desired product on the sample (Reyntjens and Puers, 2001). This procedure can be repeated to build thicker films and material can be deposited in arbitrary geometries.

Sample preparation using the so-called in situ lift-out method relies heavily on both CVD deposition and milling of material. Figure 6 show snapshots of the preparation of the sample used for the experiment discussed in Section 4.2.3. The sample comprise a 7 µm layer of Sn deposited on a Cu substrate using electron beam evaporation. Prior to the FIB preparation, the sample was left to age in ambient conditions for 12 months to give time for whiskers to form. Figure 6a shows the whisker selected for lift-out. A cylindrical sample with diameter 25 µm centred on the whisker will be lifted-out. In the first step, shown in Figure 6b, protective walls of Pt has been deposited to prevent redeposition of material on the whisker and the sample surface. The next step is to mill trenches around the region being lifted out. This is done by tilting the sample so that the ion beam is perpendicular to the surface. The end result can be seen in Figure 6c. The edges of both the sample and the trench are wavy due to redeposition of material sputtered away from the trenches. This step is relatively time-consuming, in this case, the milling took several hours. It is seen that parts of the Pt wall have collapsed or been milled away. This can be explained by sample, or beam, drift during the long (unsupervised) milling. After the trenches are milled, the sample is a free-standing cylinder, easily accessible from all sides. However, it is still attached to the substrate. The stage is now tilted so that the ion beam hits the sample at an angle of 52°; this allows ions to mill away material from the bottom of the cylinder. Repeating this process from two sides gives the bottom of the sample a triangular shape and releases it partially from the substrate. Figure 6d shows a snapshot of this procedure. It is essential to leave the sample partially attached to the substrate until it is fixated to the micromanipulator to prevent it from coming loose in an uncontrolled way. The final, and most critical, step is to lift the milled out cylinder from the substrate and attach it to a pin. This is achieved using a micromanipulator needle which is carefully positioned close to one side of the cylinder. The

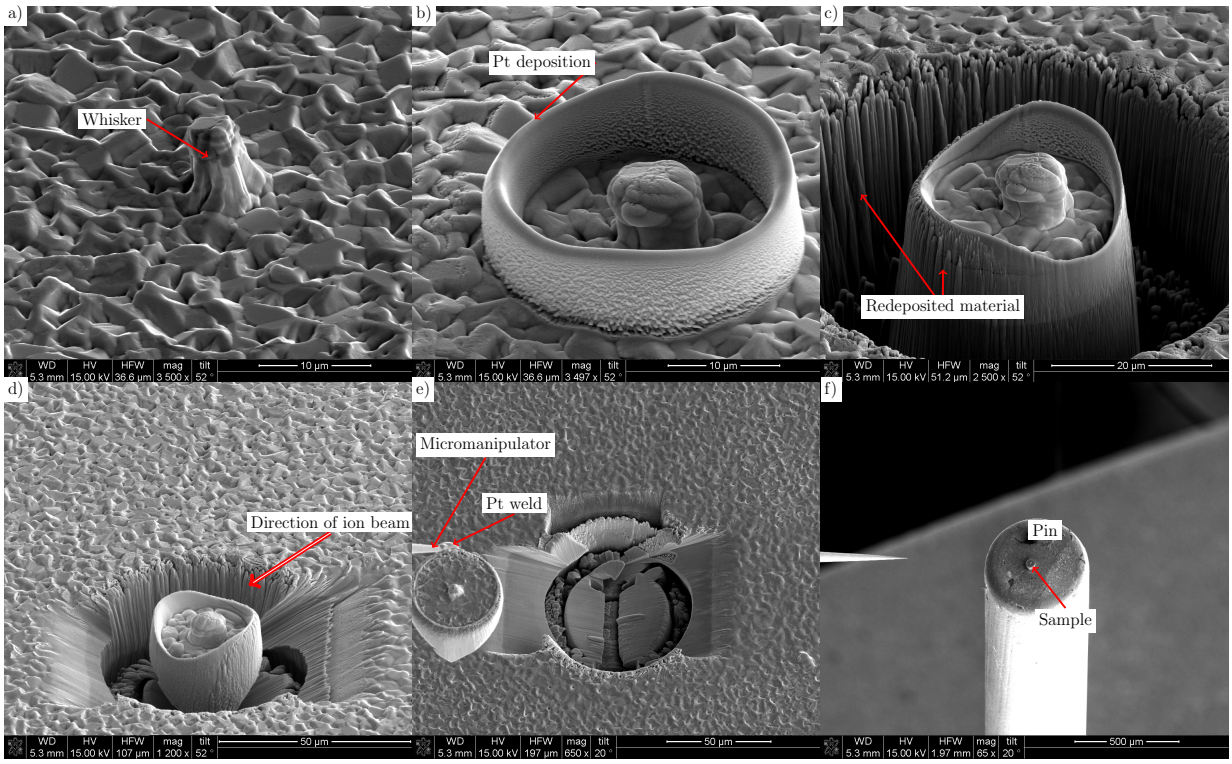

Figure 6: SEM images showing the different stages during FIB lift-out. a): The whisker before FIB milling started. b): Protective Pt walls deposited in a circle with diameter 25 µm around the whisker. c): Trenches are milled with the ion beam perpendicular to the surface. d): For the undercut, the sample is rotated so that the ion beam hits at an angle. e): The free sample is attached to a micromanipulator needle and lifted from the substrate. f): The finished sample mounted on a pin. Note that e) and f) show a different sample than the other images.

micromanipulator is welded to the sample using Pt deposition. The stage is then lowered so that the sample is hanging from the micromanipulator as seen in Figure 6e. Finally the sample is attached to a pin as seen in Figure 6f using additional Pt deposition and the lift-out is complete.

4.1.1 Ion beam imaging

As mentioned above, secondary electrons are emitted when the ion beam interacts with the sample. This means that it is possible to use the FIB for imaging, in much the same way as with an SEM. Figure 7 shows a cross-section of a tin coating on a copper substrate prepared using FIB milling, imaged both with ion-induced secondary electrons (ISE) and secondary electrons (SE). Individual grains of both copper and tin are easily identified in the ISE image, Figure 7a, but are much harder to identify in the SE image, Figure 7b. This grain contrast is caused by a phenomenon known as ion channelling. When the crystal is oriented so that the atoms are aligned along the beam direction, the ions will "channel" between lattice planes and fewer secondary electrons are generated close to the surface, and the grain will appear dark in the ISE image (Giannuzzi et al., 2005). Consequently, grains

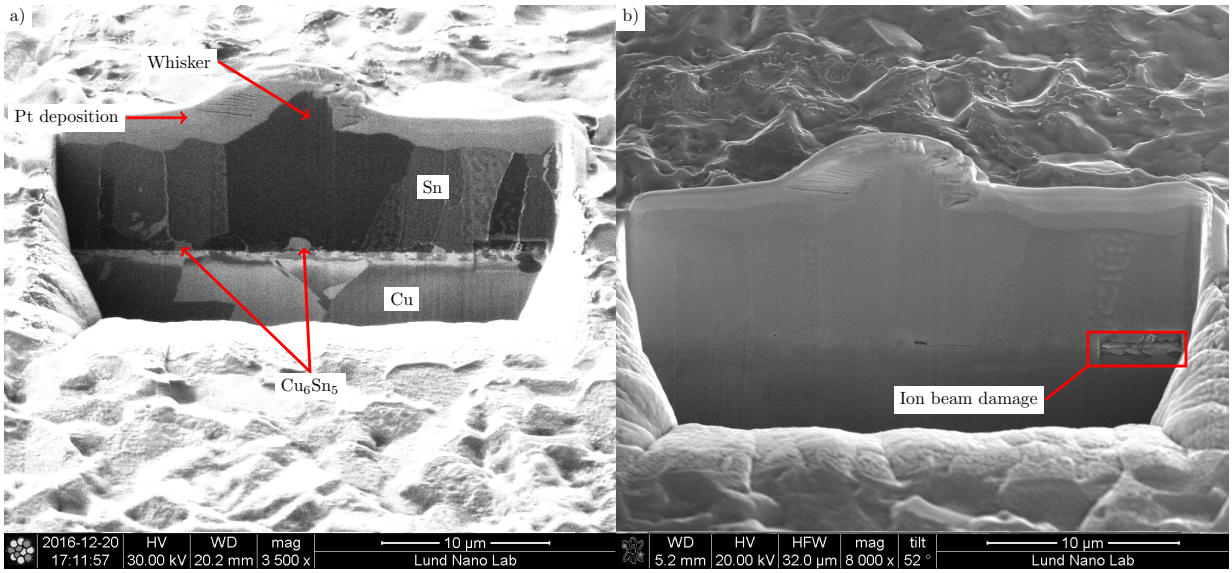

Figure 7: The same cross-section imaged using (a) ion-induced secondary electrons (ISE) and (b) secondary electrons (SE). Individual grains can be easily distinguished in the ISE image due to the higher channelling contrast.

which are oriented at a high angle relative to the ion beam will generate many secondary electrons and appear bright in the ISE image. Channelling contrast can be easily separated from contrast due to the density of the material since it depends on the orientation of the sample and will change when tilting or rotating the sample stage (Volkert and Minor, 2007). Due to the sputtering effect, imaging with the ion beam will cause damage to the sample. This is evident in the region marked in Figure 7b (this region was used for focusing and for adjusting contrast and brightness).

4.2 X-ray diffraction

More than a century ago, Max von Laue and co-workers first observed x-rays diffracting from crystals (Friedrich et al., 1913). Since then x-ray diffraction (XRD) has been one of the most important tools in materials science. One common use of XRD is to determine the arrangement of atoms in crystalline materials. It can be shown that, for a given scattering geometry, diffraction only occurs in directions which satisfy the Laue conditions (Als-Nielsen and McMorrow, 2011):

$$\boldsymbol{q} = h\boldsymbol{a}_1^* + k\boldsymbol{a}_2^* + l\boldsymbol{a}_3^* = \boldsymbol{\Omega}\boldsymbol{U}\boldsymbol{B}\begin{bmatrix} h \\ k \\ l \end{bmatrix}, \tag{23}$$

where $\boldsymbol{q}$ denotes the scattering vector, $\boldsymbol{a}_i^*$ are the reciprocal lattice vectors of the crystal, h, k, l are the Miller indices of the diffracting plane, $\boldsymbol{\Omega}$ is a matrix describing the mapping between the sample frame and the lab frame, which is known from the geometry of the setup, and $\boldsymbol{UB}$ describes the mapping between the sample frame and the reciprocal frame of the crystal (Busing and Levy, 1967).

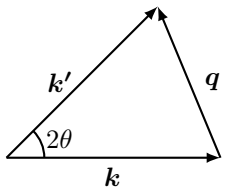

Figure 8: Illustration of the scattering vector $\boldsymbol{q}$ and the diffraction angle 2θ. The wavevectors for the incoming and diffracted beams are denoted $\boldsymbol{k}$ and $\boldsymbol{k'}$, respectively.

The reciprocal lattice vectors are defined as

$$\begin{aligned}\boldsymbol{a}_1^* &= \frac{\boldsymbol{a}_2 \times \boldsymbol{a}_3}{\boldsymbol{a}_1 \cdot (\boldsymbol{a}_2 \times \boldsymbol{a}_3)} \\ \boldsymbol{a}_2^* &= \frac{\boldsymbol{a}_3 \times \boldsymbol{a}_1}{\boldsymbol{a}_2 \cdot (\boldsymbol{a}_3 \times \boldsymbol{a}_1)} \\ \boldsymbol{a}_3^* &= \frac{\boldsymbol{a}_1 \times \boldsymbol{a}_2}{\boldsymbol{a}_3 \cdot (\boldsymbol{a}_1 \times \boldsymbol{a}_2)},\end{aligned} \tag{24}$$

where $\boldsymbol{a}_i$ are the lattice vectors defined in Figure 2. The scattering vector is given by

$$\boldsymbol{q} = \boldsymbol{k'} - \boldsymbol{k}, \tag{25}$$

where $\boldsymbol{k}$ and $\boldsymbol{k'}$ denotes the wavevectors for the incoming and the diffracted beams, respectively, as illustrated in Figure 8. The scattering is assumed to be elastic and the length of the wavevectors is inversely proportional to the wavelength of the x-rays, λ, i.e.,

$$|\boldsymbol{k}| = |\boldsymbol{k'}| \propto \frac{1}{\lambda}. \tag{26}$$

In a diffraction experiment, the angle 2θ, shown in Figure 8, and the out-of-plane angle η are measured for many diffraction peaks. These angles define the wavevector of the diffracted beam, $\boldsymbol{k'}$. The scattering vectors for all observed diffraction peaks can then be determined from Equation (25). The reciprocal lattice vectors of the measured crystals are then determined by fitting $\boldsymbol{UB}$ to the observed scattering vectors using Equation (23). The $\boldsymbol{UB}$ matrix can be split into two parts: $\boldsymbol{U}$ which describes the orientation of the measured crystal, i.e. the mapping between the sample frame and a frame attached to the crystal, and $\boldsymbol{B}$ which describes the reciprocal unit cell parameters, i.e. a mapping between the crystal frames in direct and reciprocal space.

When the unit cell parameters and the crystal orientation are known, the elastic strain tensor, in the sample frame, is determined by

$$\boldsymbol{\varepsilon}^e = \boldsymbol{U}\left(\frac{1}{2}\left(\boldsymbol{A}\boldsymbol{A}_0^{-1} + \left(\boldsymbol{A}\boldsymbol{A}_0^{-1}\right)^T\right) - \boldsymbol{I}\right)\boldsymbol{U}^T, \tag{27}$$

where $\boldsymbol{I}$ is the identity matrix and $\boldsymbol{A}$ is formed from the unit cell parameters,

$$\boldsymbol{A} = \begin{bmatrix} a & b\cos\gamma & c\cos\beta \\ 0 & b\sin\gamma & -c\sin\beta\cos\alpha^* \\ 0 & 0 & c\sin\beta\sin\alpha^* \end{bmatrix}, \tag{28}$$

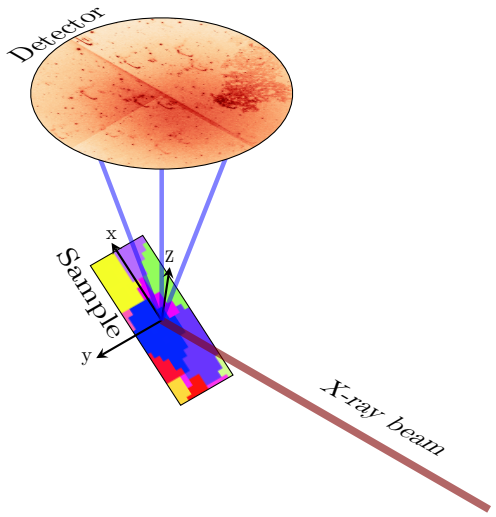

Figure 9: Illustration of the setup for a scanning Laue microdiffraction experiment.

$\boldsymbol{A}_0$ is constructed in the same way as $\boldsymbol{A}$, but using lattice parameters of a reference crystal.

4.2.1 Laue microdiffraction

In Laue diffraction a polychromatic beam is used and therefore the wavelengths of the diffracted beams are unknown. This lack of wavelength information means that it is not possible to determine the length of the scattering vector $\boldsymbol{q}$. Without this knowledge, Equation (23) can only be used to determine the reciprocal lattice vectors up to a constant factor. This limitation means that Laue diffraction will only provide the relative unit cell parameters, i.e., the shape of the unit cell can be determined, but not its volume. Regarding strain measurements, this limitation means that only deviatoric strains can be measured. The volumetric part may be approximated using some assumption, e.g., by assuming a vanishing out-of-plane stress such as in Paper B.

The setup for a Laue microdiffraction experiment is illustrated in Figure 9. A focused, polychromatic, beam is raster scanned over a sample which is mounted at an angle of 40°. The resulting diffraction patterns are measured by a 2D detector placed above the sample, i.e., in reflection mode. The diffraction patterns typically contain peaks belonging to several grains located in the volume probed by the x-ray beam. The grains on the surface of the sample are mapped by assuming that the brightest diffraction peak belongs to the surface grain.

Laue microdiffraction has been used to study tin whiskers on multiple occasions. Choi et al. (2003) used Laue diffraction together with the plane stress assumption to map out the biaxial stress field around a tin whisker. They found that the stress field was highly inhomogeneous and also saw stress gradients around the whisker root. A similar study, but with higher spatial resolution, was presented in Sobiech et al. (2009). The strain field in their study was more homogeneous than in the study by Choi et al. (2003). Negative gradients in strain were observed when radially averaging around the whisker root. This observation leads to a hypothesis that it is these strain gradients, rather than whether the stress is compressive or tensile, that are responsible for whisker growth. In a study by Sarobol et al. (2013a,b) it was found that the whiskers grew from grains with high misorientation

relative to other grains in the coating. This misorientation was postulated to lead to high localised elastic strain and strain energy density. After nucleation of the surface defect (whisker or hillock), the strain energy is relaxed. These claims were supported by finite element simulations. All of these studies were performed after the whisker had formed, it is therefore not clear whether the observations are the cause of whisker growth or a consequence of it.

In an in situ study by Pei et al. (2016), Laue microdiffraction was used together with fluorescence mapping in an attempt to observe the nucleation of defects on the surface of a tin coating. Unfortunately, no whisker nucleated in the studied regions; they did, however, observe the formation of a hillock. Contrary to what was observed in Sarobol et al. (2013a) the hillock grew from a grain with an orientation similar to the average texture of the sample. The hillock grain did have a lower magnitude of stress and lower strain energy density than its surroundings, however, no long-range stress gradients were seen. This contradicts the results in Sobiech et al. (2009). It should be noted that the growth mechanisms of hillocks are not necessarily the same as for whiskers.

In the study presented in Paper B, Laue microdiffraction was used to study the evolution of the same two tin whiskers during long-term ageing. Three measurements were conducted on one of the whiskers; after 4, 11, and 21 months of ageing, the second whisker was measured after 11 and 21 months. It was found that the orientation of the whisker shown in Figure 10a was similar to the surrounding grains. The orientation of the second whisker was however unique, cf. Paper B. In the map of the hydrostatic stress, Figure 10b, it is seen that the stress field is highly inhomogeneous. The stress in the whisker root (marked by the black circle) is becoming increasingly tensile with time. This shows that whisker growth indeed acts as a relaxation mechanism for compressive stresses. In the stress fields, it is possible to identify ridges of compressive stress stretching out from the neighbourhood of the whisker root to the surrounding grains. Within these ridges the stress gradient will drive diffusion of tin to the nearby grain boundaries, from there atoms make their way to the root of the whisker through grain boundary diffusion. This process is illustrated by the green lines and arrows in Figure 10b. As mentioned above, whisker growth is believed to be driven by radial gradients in compressive stress. The observation of the ridges, rather than a more homogeneous radial gradient, indicate that the compressive stress gradients are much more localised than previously expected.

The dotted circles in Figure 10 indicate a grain which is nucleating and growing with time. It is located in the boundary between a grain with tensile stress and a grain with compressive stress, i.e., in this location there is a large gradient in the hydrostatic stress. With time the stress in the grain under compression is relaxed, and the new grain is growing. SEM investigations revealed that the circled grain corresponds to a feature on the surface that was not seen in the first measurement. This feature is either a very short whisker, or what is described as a *popped* grain in Susan et al. (2013). The popped grains are described as whiskers which nucleated but, for some reason, did not grow to an appreciable length (Susan et al., 2013).

4.2.2 Differential aperture x-ray microscopy (DAXM)

To obtain 3D resolution in a Laue microdiffraction experiment, a thin wire, made from an absorbing material such as tungsten (W), can be scanned above the sample surface. For each position of the wire, a diffraction pattern is measured. By tracking the changes to the diffraction pattern as a function of the wire position, each diffraction peak can be reconstructed as a function of depth. This method is

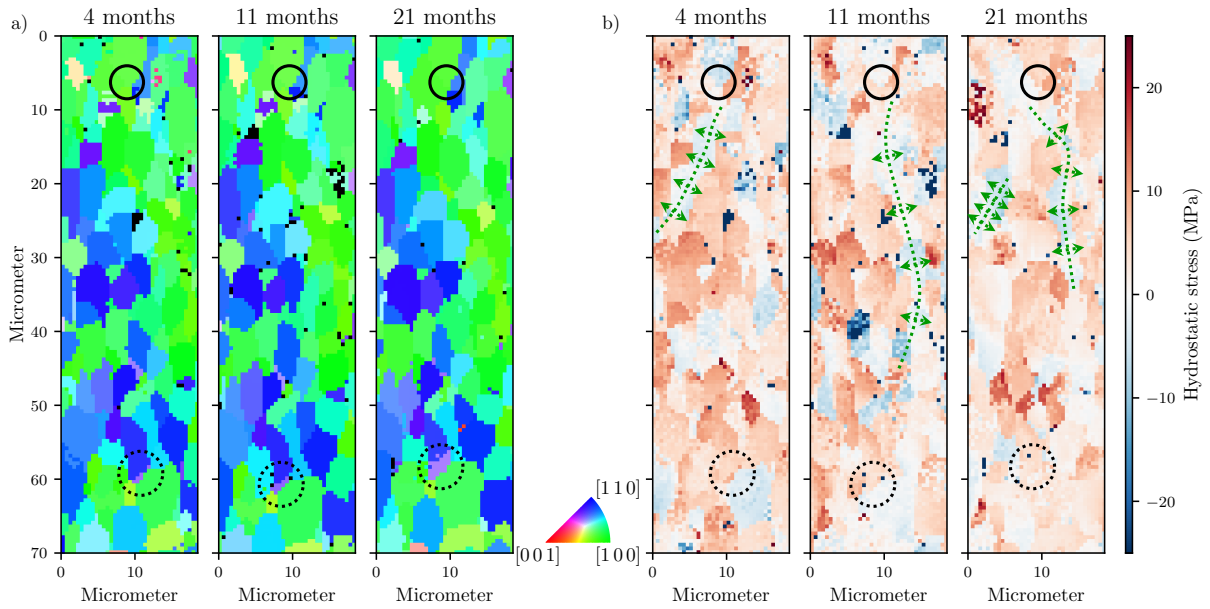

Figure 10: Evolution of the microstructure around a tin whisker during ageing captured using Laue microdiffraction. The black circle indicate the position of the whisker root. The dotted circle shows the location of a nucleating whisker. a): Grain orientation coloured by the inverse pole figure of the sample normal. b): Hydrostatic stress calculated by assuming $\sigma_{zz} = 0$. The green lines mark ridges of compressive stress leading to the whisker root. The green arrows illustrate how tin atoms diffuse from the ridges to nearby grain boundaries and then to the root of the whisker.

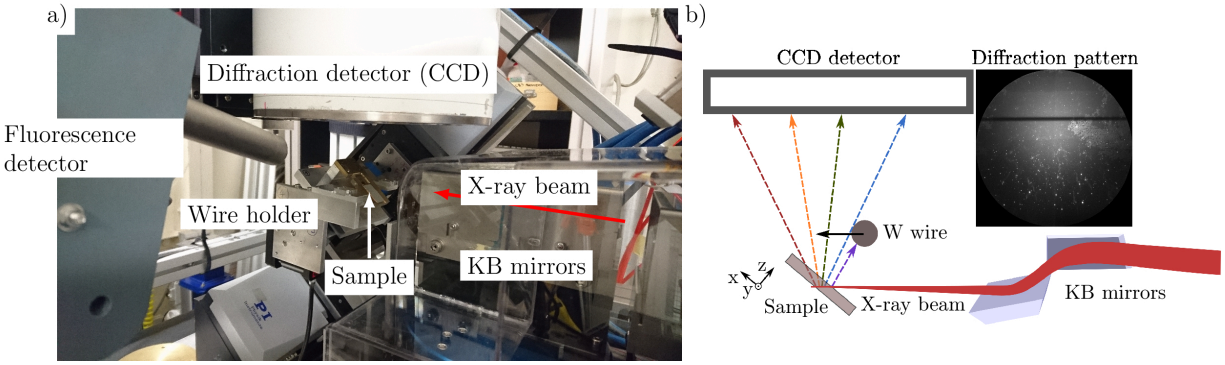

Figure 11: a): Photograph of the DAXM set-up at BM32 of the ESRF. The red arrow indicates the incoming x-ray beam. b): Illustration of the DAXM set-up. The W wire is seen as a horizontal shadow on the diffraction pattern. The set-up for conventional Laue microdiffraction is the same except for the W wire which is removed.

called Differential Aperture X-ray Microscopy (DAXM) and was developed by Larson et al. (2002) at the Advanced Photon Source (APS). An illustration of the set-up for a DAXM experiment and a photo of the microdiffraction set-up at BM32 (Ulrich et al., 2011) of the European Synchrotron Radiation Facility (ESRF) is shown in Figure 11. The advantage of DAXM compared to other 3D diffraction techniques capable of resolving intragranular variations, such as scanning 3DXRD discussed below, is that there are fewer restrictions on which type of samples that can be measured. Since DAXM is performed in reflection mode, there is no need for the x-rays to pass through the sample, this allows for large samples to be scanned. There is also no need for rotation of the sample which facilitates in situ experiments such as tensile testing. DAXM is also less sensitive to spot overlaps and mosaic spread of the diffraction spots compared to other techniques, which means that highly strained and plastically deformed samples can be measured. As with most scanning based techniques, the main drawback of DAXM is the long measurement time. For high depth resolution, the wire must be scanned at many positions along the beam. This means that to reconstruct even a single line in depth thousands of diffraction patterns must be measured. Clearly, this limits the size of the region that is feasible to measure. One approach to reducing the measurement time is to, instead of a single wire, use an array of wires (Marijon, 2017). In the best case scenario, an array of n wires would reduce the measurement time by a factor of n.

The first three-dimensional reconstruction of the microstructure and the strain field around a tin whisker is presented in Paper C. In this experiment DAXM, with a single wire, was used to study the grain orientation and deviatoric strain around the whisker shown in Figure 1a. The reconstruction of the microstructure is shown in Figure 12. Due to the many wire positions needed to get an in-depth resolution of 1 µm, each position on the sample took three hours to measure. For this reason, it was not possible to scan a full volume with depth resolution. Instead, two perpendicular planes, intersecting at the root of the whisker was scanned. It should be noted that the DAXM setup on BM32 has recently been upgraded to facilitate much faster measurements, among other upgrades a multi-wire setup has been developed. From the reconstruction of the data, it is evident that the tin grains are columnar, with only one grain throughout the thickness of the coating. The deviatoric

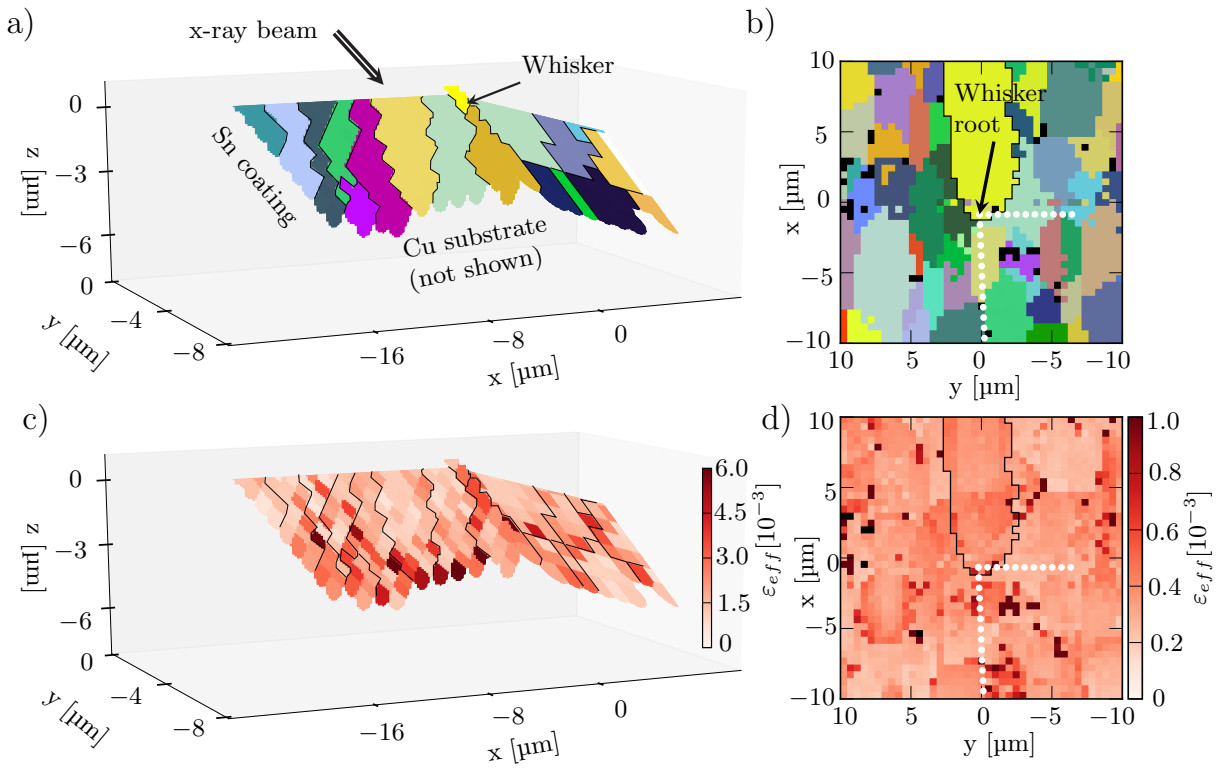

Figure 12: Reconstruction of the grain structure and the effective deviatoric strain around a tin whisker using DAXM. The 3D reconstructions show two perpendicular planes intersecting in the whisker root (illustrated by the arrow). The white dots in the 2D maps (b and d) indicate the positions scanned using DAXM. a): 3D reconstruction of the grain orientations coloured by Euler angles. b): 2D map of the grain orientations in the region around the whisker obtained by scanning Laue microdiffraction. c): 3D reconstruction of the effective deviatoric strain. d): 2D map of the effective deviatoric strain.

strain is highest deep in the coating, close to where the IMC is located. The deviatoric strain is a measure of the distortion of the crystal lattice and can, therefore, be seen as an indication of plastic deformation. The high deviatoric strain would imply that the growth of the IMC generates enough stress to deform the bottom of the coating plastically. This is in agreement with the simulations discussed in Section 3.1.

4.2.3 Scanning 3D x-ray diffraction (3DXRD)

Three dimensional x-ray diffraction (3DXRD) can be used to map out grain orientations, centre of mass positions, and strain in polycrystalline samples (Poulsen, 2004). In contrast to the Laue diffraction discussed in Section 4.2.1, in 3DXRD a monochromatic x-ray beam is used. In terms of strain measurements, a monochromatic beam is advantageous as the full strain tensor can be accessed without making any assumptions about the stress state. 3DXRD is done in transmission mode which

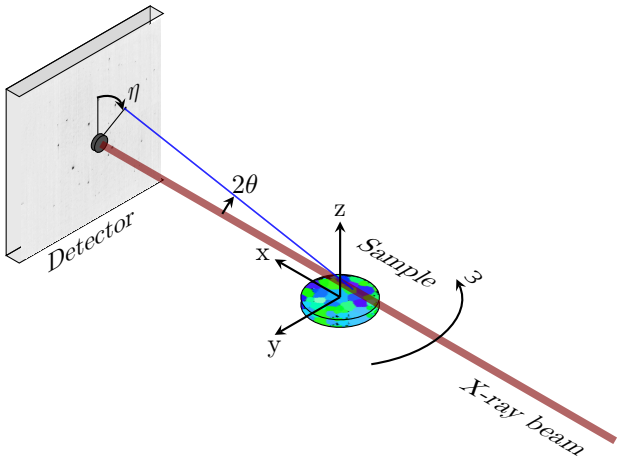

Figure 13: Illustration of the setup for a 3DXRD experiment using a focused pencil beam. The sample is raster scanned in the $y - z$ plane and diffraction patterns are collected for ω angles in the range 0 to 180°. The position of the diffraction peaks are determined by the angles $(2\theta, \eta)$.

means that the energy of the beam needs to be high enough to penetrate the sample, typically energies in the range of 50 to 100 keV are used (Jensen et al., 2006). Using high energies has the advantage that the diffraction angles are smaller, such that a detector of finite size will be able to record a large number of diffracted beams.

The setup for a 3DXRD experiment is illustrated in Figure 13. A cylindrical sample is mounted on a rotation stage (ω) and illuminated by the x-ray beam. For each ω setting, diffracted beams from lattice planes which satisfy Equation (23), or equivalently the Bragg condition, are measured on a high-resolution area detector. To probe the complete crystal structure within the illuminated volume the sample is rotated, and diffraction patterns are measured at ω-angles in the range 0 to 180°. Typically, the illuminating beam is shaped into one of the following three configurations:

- Box beam, which illuminates the whole sample at once. This configuration allows for fast measurements and is therefore well suited for in situ experiments. With this beam shape, the orientation and strain will be averaged over the full volume of each grain.

- Line beam, which illuminates a horizontal slice of the sample. To obtain resolution in three dimensions several slices are stacked together. Here the orientation and strain are averaged over the cross-section of the grain in each slice. For large enough grains, it is possible to capture intragranular variations of the unit cell parameters and the grain orientation in the vertical direction.

- Pencil beam, which illuminates only a small part of the sample. In this configuration, it is necessary to scan the sample across the beam along two translational and one rotational axis. This makes measurements rather time-consuming. The advantage is that the results are not averaged, i.e., it is possible to capture strain and orientation variations in all three dimensions. This method is sometimes referred to as scanning 3DXRD (Hayashi et al., 2015).

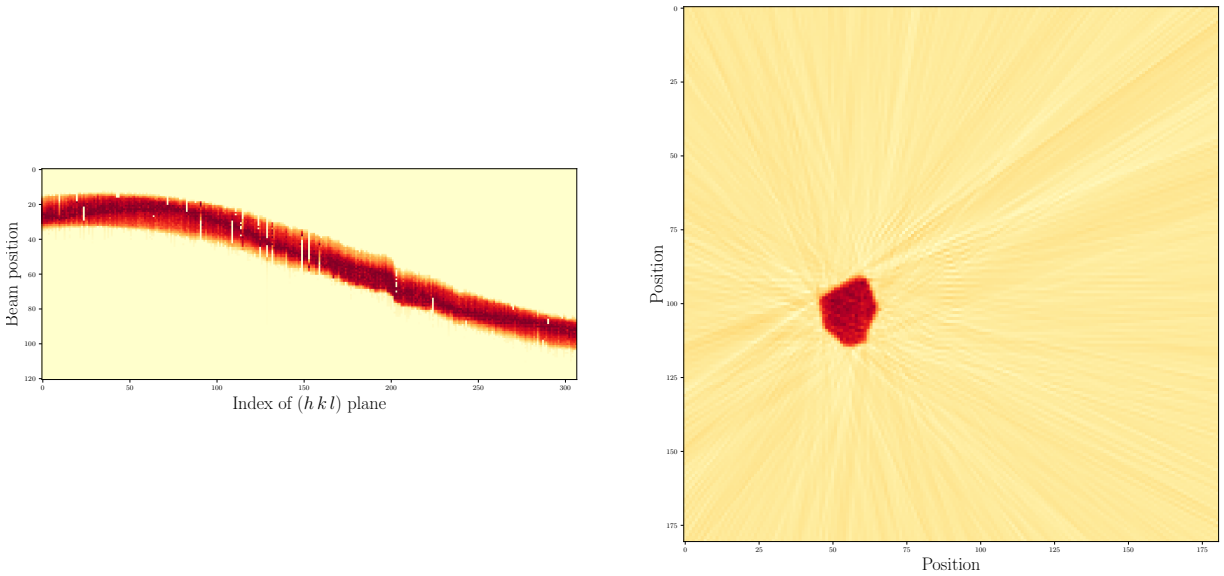

Figure 14: Left: Sinogram of data belonging to one tin grain. Right: Reconstruction of the shape and position of the grain, using the filtered backprojection algorithm.

The average grain orientations and lattice parameters for each grain of the sample are obtained by fitting Equation (23) to the measured data, taking the Ω matrix as

$$\boldsymbol{\Omega} = \begin{bmatrix} \cos\omega & -\sin\omega & 0 \\ \sin\omega & \cos\omega & 0 \\ 0 & 0 & 1 \end{bmatrix}. \tag{29}$$

For measurements with a pencil beam, intragranular variations of strain and orientation can be reconstructed by further data analysis. The first step in the refinement is to build a sinogram of the total intensity of the diffraction peaks belonging to each grain. From the sinograms, the shape and position of all grains can be determined using a filtered back-projection algorithm (Bonnin et al., 2014; Poulsen and Schmidt, 2003). The sinogram of one grain and the corresponding reconstruction of the shape and position is shown in Figure 14. Repeating the reconstruction for all grains, and at all z, results in a 3D grain map of the sample.

In the next step of the refinement, the $\boldsymbol{UB}$ matrix is fitted locally in each voxel of the reconstructed grain map. Following Hayashi et al. (2015) it is noted that, for a given beam position y and ω, the beam will illuminate a point $Q(x_s, y_s)$ located somewhere in the sample $x - y$ plane if

$$y(\omega) = \sqrt{x_s^2 + y_s^2}\cos\left(\omega + \arctan\frac{x_s}{y_s}\right). \tag{30}$$

Equation (30) is used, together with the knowledge of which grain $Q(x_s, y_s)$ is located within, to extract all data containing diffraction events from the current voxel and the current grain. The extracted data will not only contain data from voxel Q but from all voxels in the same grain illuminated by the beam settings given by Equation (30). The dataset will, however, be dominated by the contribution

from Q since that is the only voxel which is illuminated in all extracted $y - \omega$ scans.The extracted data is then fitted to a forward model of the diffraction to obtain a refined $\boldsymbol{UB}$ matrix for voxel Q.

In Paper D, the first 3DXRD experiment on a tin whisker is presented. The experiment was carried out using the pencil beam configuration described above. The preparation of the sample was discussed in Section 4.1 and SEM images of the sample are shown in Figure 6. During the experiment, the sample was scanned in its fabricated state and again after being heat treated at 150 °C for three hours. Figure 15 show 3D reconstructions of the grain structure around the tin whisker in both the original and the heated state. The tin grains are coloured based on their orientation, and the black grains are Cu_6Sn_5. A similar, columnar, grain structure as in the DAXM experiment, cf. Figure 12, is observed. It is also seen that the grain boundaries of the whisker are oblique. For a biaxial state of stress, it can be shown by simple trigonometry that the stress in oblique grain boundaries is always lower in magnitude compared to if the grain boundary was vertical. In the whisker growth theory proposed by Smetana (2007) it is assumed that some recrystallisation mechanism forms grains with oblique grain boundaries, the stress gradient then drives diffusion of atoms towards the newly formed grain which will grow upwards, and become a whisker, due to grain boundary sliding. Stress relaxation in oblique grain boundaries can also explain why very few whiskers are forming in coatings of lead-tin alloys. These alloys do not have the columnar grain structure that coatings of pure tin do. This allows stresses to be accommodated in the already present oblique grain boundaries.

From Figure 15 it is also seen that coarsening of some tin grains took place during the heat treatment. One example of this is seen in the region marked by the dotted ellipse below the whisker grain. In the original state, this region consists of seven tin grains with different orientations – one of them being the whisker grain – and one grain of Cu_6Sn_5. After heat treatment, the same region contains only four tin grains and the grain of Cu_6Sn_5. The dark blue and purple grains have coarsened and consumed the two, smaller, green grains. The purple grain has also grown in the vertical direction and is almost reaching the sample surface. A 3D map of the crystallographic phases present in the tin coating is shown in Figure 16. The heat treatment promoted the growth of the, already existing, grains of Cu_6Sn_5 as well as nucleation of new grains of the intermetallic phase. Interestingly, the largest IMC grain is located right below the whisker in the centre of the sample. The growth of this IMC grain will give rise to compressive stresses close to the whisker root.

Figure 17a shows a 3D reconstruction of the hydrostatic stress in the tin coating, in its original state. Compressive stress is coloured in shades of blue and tensile stress is coloured in shades of red, yellow indicates Cu_6Sn_5. The stress is calculated using the average lattice parameters of the whisker as a stress-free reference. It is seen that the stress in the coating is mainly compressive, the few regions with tensile stresses are located in grain boundaries or at the surface. There are variations of stress within individual grains. This shows the usefulness of the scanning based approach as these would not be captured using standard 3DXRD; it also suggests that the reconstruction algorithm is working as intended. In Figure 17b, the hydrostatic stress is radially averaged in 3D, with distance zero taken in the centre of the whisker grain at level with the sample surface, the part of the whisker above the surface is not included in the averaging. The curve starts at a slightly tensile value, the stress then becomes increasingly compressive over a distance of approximately 4 µm before becoming more tensile. After 6 µm the stress becomes more compressive again, this continues to the edge of the sample. The initial gradient would drive diffusion of tin atoms towards the root of the whisker from within 4 µm of the whisker root. Due to the large volume of tin whiskers and the relatively

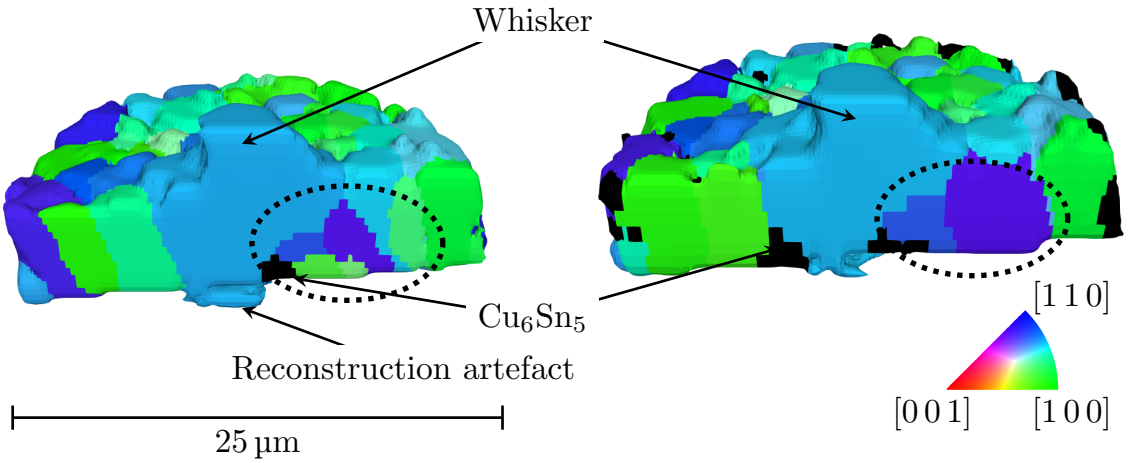

Figure 15: 3D reconstruction of the grain structure around the tin whisker investigated using 3DXRD. The tin grains are coloured based on their orientation using the inverse pole figure colourmap. Black grains corresponds to the Cu_6Sn_5 phase. The dotted ellipse marks a region where coarsening of tin grains occur. Left: Before heat treatment. Right: After heat treatment.

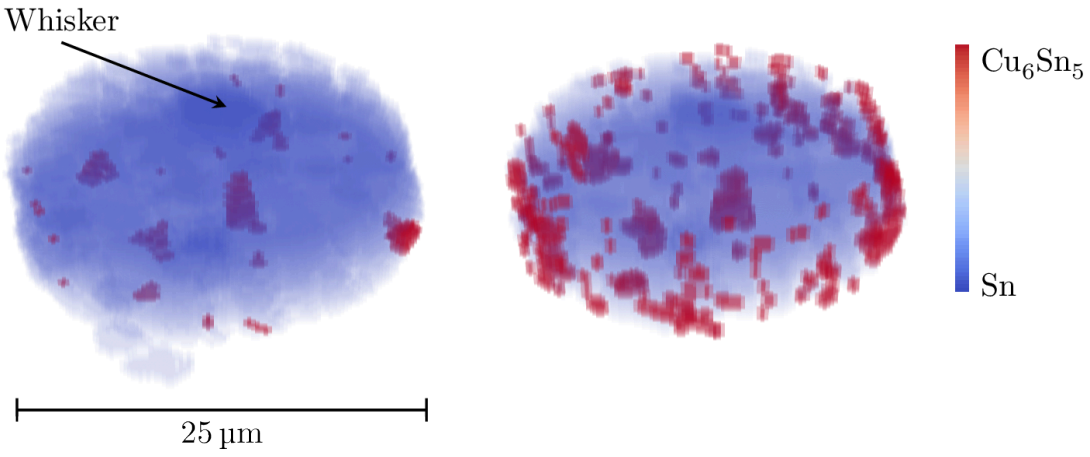

Figure 16: 3D reconstruction of the Cu_6Sn_5 grains (red) within the tin coating (blue). The grains are made opaque to allow for depth resolution. Left: Before heat treatment. Right: After heat treatment.

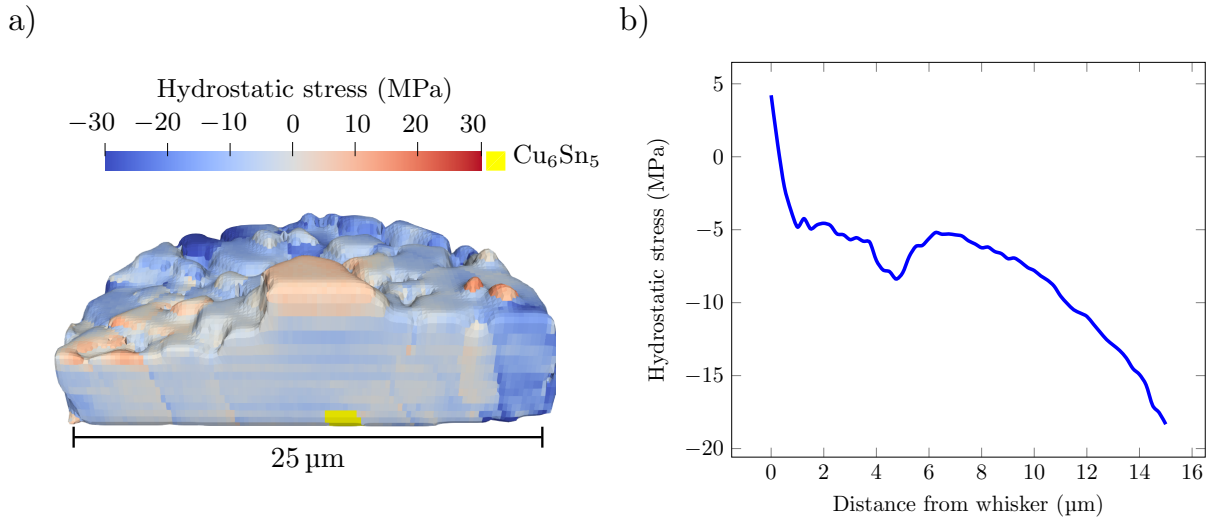

Figure 17: a): 3D reconstruction of the hydrostatic stress field before heat treatment. b): Radially averaged hydrostatic stress as a function of distance from the whisker root.

short stress gradient observed, it is unlikely that all material making up the whisker originates from the region with the negative stress gradient. Radial diffusion of atoms towards the whisker root is therefore probably not the only driving force for whisker growth. A more reasonable explanation is that whisker growth is driven by a combination of radial diffusion from a small region near the whisker root and long-range diffusion from ridges of compressive stress, such as those seen in Figure 10. It can be envisaged that the ridges are supplying material to the region close to the whisker through grain boundary diffusion, this material then diffuses radially to the root of the whisker. The evolution of the ridges means that the supply of material comes from a large region of the coating, this can explain why whiskers seem to grow without any apparent depletion of material in other parts of the coating.

5 Summary

Tin whiskers can cause significant problems by short-circuiting electronic components. The mechanisms responsible for whisker formation are not yet fully understood. A theoretical understanding of these mechanisms is key to finding a solution to the problem of tin whiskers. The work presented in this thesis aims at taking a step towards this understanding by x-ray diffraction experiment as well as numerical simulations. Both the experiments and the simulations are focused on characterising the microstructure and the stress field in tin coatings.

A phase field model capable of simulating the growth of the Cu_6Sn_5 phase have been developed. The model can be used to simulate the growth of the IMC and how this generates stresses in the tin coating. This model is one of very few phase field models that combines diffusion with elasticity and plasticity.

The experimental work in this thesis is focused on characterising the microstructure and the stress

field around a tin whisker, in 3D. This is something that has not been achieved before. The evolution of the microstructure around tin whiskers during long-term ageing was also investigated. Based on the results of the experiments it is suggested that whisker growth is driven by a combination of radial diffusion from the nearby region and long-range diffusion from certain ridges of compressive stress.

6 Future work

Much more work remains to be done to fully understand and be able to predict whisker formation and growth. A key component in this endeavour is the coupling between experiments and numerical models. One example of this is presented in Zhang et al. (2017) where the model parameters of a phase field model are determined by minimising the difference between the model and an x-ray tomography experiment. A similar approach could be used for the phase field model in this thesis by using the results from the 3DXRD, or the DAXM, experiments. With a model that matches the experiments, it is possible to use simulations to draw conclusions regarding things the experiments cannot capture. The model could also be used to make predictions regarding for example how the orientation of the tin grains influence the stress field.

One obvious limitation of the phase field model in this thesis is that it is implemented in 2D. Clearly whisker growth is a 3D problem so to simulate it satisfactory one would need a 3D model. Another drawback is that the model does not include the actual whisker. To include the whisker in the model it is necessary to include the surface of the sample and the air above. This is however not a trivial exercise. With minor modifications, the model could also be used to simulate other phenomenon related to electronic components, such as electromigration or formation of Kirkendall voids.

On the experimental side, it would be interesting to repeat the 2D Laue study on a larger number of whiskers. Doing this it would be possible to determine whether the ridges of compressive stress are always present, or if whiskers can grow without them. It could also be possible to characterise any plastic deformation in the coating by analysing the shape of the measured diffraction peaks. This could e.g. give an estimation of the number of geometrically necessary dislocations, which could be directly compared to the results of the phase field model. Capturing the nucleation of a whisker in 3D would shed light on how the oblique grain boundaries are formed and what role, if any, they play during whisker growth. This could potentially be achieved by encouraging whiskers to form in specific regions using for example nano-indentation to induce additional compressive stress near the measured region. Another opportunity is to improve the spatial, and strain, resolution of the experiments. This could, of course, be done using better focusing of the x-ray beam and use of a detector with higher resolution. It could also be possible by a technique which utilises the increased coherency of next-generation synchrotrons, such as coherent diffraction imaging or Bragg ptychography.

7 Summary of the appended papers

Paper A: A multiphase field model combining diffusion with elasticity and plasticity was developed. The governing equations were derived in a thermodynamically consistent way using the concept of microforce balance laws. The model was used to simulate the growth of Cu_6Sn_5 during ageing at

room temperature. Results from the simulations suggest that compressive stress develops in the Sn layer due to the volume change associated with the IMC formation. Furthermore, it was found that plastic deformation occurs in both the Cu and the Sn layers. It was also found that the morphology of the IMC grains changes from scallop-like to planar. All of this is in good agreement with experimental findings.

Paper B: The evolution of the microstructure around two whiskers was studied over a period of 17 months. Using Laue microdiffraction, together with an assumption of vanishing out-of-plane stress, it was possible to identify ridges of compressive stress leading to the whisker root. These ridges evolve with time and are believed to drive diffusion of tin towards the whisker root. The orientation of one of the whiskers was found to be similar to the surrounding grains in the coating, the orientation of the second whisker, however, was unique. A new whisker, or popped grain, nucleated in a region with a large gradient in compressive stress. With time the compressive stress nearby was relaxed, and the growth of the new whisker stopped.

Paper C: DAXM was used to measure grain orientations and deviatoric strain around a tin whisker in 3D. Due to the slow detector used it was not possible to measure a full volume in 3D. Instead, two perpendicular lines centred on the whisker root were scanned with DAXM so that depth resolution was obtained on two planes. The results show that the tin grains surrounding the whisker are columnar and that the grain boundaries of the whisker grain are inclined approximately 50° with respect to the sample surface. Strain gradients through the depth of the tin layer were found and explained by the growth of Cu_6Sn_5 in the interface between the Cu substrate and the Sn coating. Formation of Cu_6Sn_5 cause a volume change that locally leads to high deviatoric strain. The high strain can lead to plastic deformation and pile-up of dislocations at the surface, causing the oxide layer to crack and a whisker to nucleate through the crack.

Paper D: Scanning 3DXRD was used to study the evolution of the microstructure around a tin whisker during heat treatment. It was found that the as-deposited tin grains were oriented such that the c-axes of the crystals were parallel to the sample surface. The few grains with a different orientation disappeared during heat treatment. The heat treatment also promoted the growth of the Cu_6Sn_5 phase. Reconstructions of the hydrostatic stress field reviled compressive stress in the tin coating, a negative gradient in hydrostatic stress extending for about 4 µm were found. This gradient will drive diffusion of nearby material to the whisker root.

A Appendix: Parameters for the crystal plasticity simulations

The parameters presented here were used for the simulations discussed in Section 3.2, all parameters are representative for the material behaviour at 150 °C. The parameters used in the phase field model for all phases and the elastic parameters of Cu and Cu_6Sn_5 are shown in Table 3. The elastic parameters for tin are given in Table 4 and parameters for the crystal plasticity model are found in Table 5, most of these parameters are taken from Chakraborty and Eisenlohr (2018).

Table 3: Parameters used for the phase field model and the elasticity models of Cu and Cu_6Sn_5.

		Cu	Cu_6Sn_5	Sn
	Elasticity (Qin et al., 2015; Hektor et al., 2016)			
E (GPa)	Young's modulus	150	112.3	
ν	Poisson's ratio	0.35	0.31	
	Interface free energy (Moelans, 2011)			
σ_{int} (J m^{-2})	Surface energy	0.5	0.5	0.5
	Chemical free energy			
A (J m^{-3})	Gibbs energy parameter	5.8501×10^9	2.4555×10^{10}	4.1436×10^{10}
B (J m^{-3})	Gibbs energy parameter	-1.378×10^9	-5.3935×10^8	2.9931×10^8
C (J m^{-3})	Gibbs energy parameter	-1.1749×10^9	-1.5313×10^9	-1.3715×10^9
$\hat{x}$ (J m^{-3})	Equilibrium molar fraction	0.144	0.413	0.995
	Diffusion (Mei et al., 1992)			
D (m^2 s^{-1})	Diffusion coefficient	4.04×10^{-26}	8.11×10^{-16}	8.05×10^{-15}
L (m^3 J^{-1} s)	Phase field mobility	3.12×10^{-9}	3.12×10^{-9}	3.12×10^{-9}

Table 4: Elastic constants, given in Voigt notation, (GPa) for tin.

C_{11}	C_{22}	C_{33}	C_{44}	C_{55}	C_{66}	C_{12}	C_{13}	C_{23}
72.3	72.3	88.4	22.0	22.0	24.0	59.4	35.8	35.8

Table 5: Parameters used in the crystal plasticity model.

Constant parameters		
$\dot{\gamma}_0^\alpha$ (s^{-1})	Initial slip rate	0.001
m	Rate sensitivity	6
$q^{\alpha\alpha}$	Self-hardening	1
$q^{\alpha\beta}$	Cross-hardening	1.4
h_0 (MPa)	Initial hardening	20
c	Hardening exponent	2
Slip system dependent parameters		
Slip system family	Saturation stress	Initial slip resistance
Plane Direction	τ_{sat} (MPa)	s_0 (MPa)
$\{1\,0\,0\}\langle 0\,0\,1\rangle$	11	8.5
$\{1\,1\,0\}\langle 0\,0\,1\rangle$	9	4.3
$\{1\,0\,0\}\langle 0\,1\,0\rangle$	11	10.4
$\{1\,1\,0\}\langle 1\,\bar{1}\,1\rangle$	9	4.5
$\{1\,1\,0\}\langle 1\,\bar{1}\,0\rangle$	10	5.6
$\{1\,0\,0\}\langle 0\,1\,1\rangle$	10	5.1
$\{0\,0\,1\}\langle 0\,1\,0\rangle$	10	7.4
$\{0\,0\,1\}\langle 1\,1\,0\rangle$	10	15.0
$\{0\,1\,1\}\langle 0\,\bar{1}\,1\rangle$	9	6.6
$\{2\,1\,1\}\langle 0\,\bar{1}\,1\rangle$	13	12.0

References

Als-Nielsen, J., McMorrow, D., 2011. Elements of modern X-ray physics. John Wiley & Sons.

Ammar, K., Appolaire, B., Cailletaud, G., Forest, S., 2009. Combining phase field approach and homogenization methods for modelling phase transformation in elastoplastic media. European Journal of Computational Mechanics/Revue Européenne de Mécanique Numérique 18 (5-6), 485–523.

Artemev, A., Jin, Y., Khachaturyan, A., 2001. Three-dimensional phase field model of proper martensitic transformation. Acta Materialia 49 (7), 1165 – 1177.

Boettinger, W., Johnson, C., Bendersky, L., Moon, K.-W., Williams, M., Stafford, G., 2005. Whisker and hillock formation on Sn, Sn–Cu and Sn–Pb electrodeposits. Acta Materialia 53 (19), 5033–5050.

Boettinger, W., Warren, J., Beckermann, C., Karma, A., 2002. Phase-field simulation of solidification. Annual Review of Materials Research 32 (1), 163–194.

Bonnin, A., Wright, J. P., Tucoulou, R., Palancher, H., 2014. Impurity precipitation in atomized particles evidenced by nano x-ray diffraction computed tomography. Applied Physics Letters 105 (8), 084103.

Brusse, J., Ewell, G., Siplon, J., 2002. Tin whiskers: Attributes and mitigation. In: 22nd Capacitor and Resistor Technology Symposium - CARTS 2002. Components Technology Inst., Inc.

Buchovecky, E. J., Du, N., Bower, A. F., 2009. A model of Sn whisker growth by coupled plastic flow and grain boundary diffusion. Applied Physics Letters 94 (19), 191904.

Busing, W. R., Levy, H. A., 1967. Angle calculations for 3-and 4-circle x-ray and neutron diffractometers. Acta Crystallographica 22 (4), 457–464.

Chakraborty, A., Eisenlohr, P., 2018. A full-field crystal plasticity study on how texture and grain structure influences hydrostatic stress in thermally strained β-Sn films. Journal of Applied Physics 124 (2), 025302.

Chason, E., Jadhav, N., Chan, W., Reinbold, L., Kumar, K., 2008. Whisker formation in Sn and Pb–Sn coatings: Role of intermetallic growth, stress evolution, and plastic deformation processes. Applied Physics Letters 92 (17), 171901.

Cheng, S., Huang, C.-M., Pecht, M., 2017. A review of lead-free solders for electronics applications. Microelectronics Reliability 75, 77 – 95.

Choi, W., Lee, T., Tu, K., Tamura, N., Celestre, R., MacDowell, A., Bong, Y., Nguyen, L., 2003. Tin whiskers studied by synchrotron radiation scanning X-ray micro-diffraction. Acta Materialia 51 (20), 6253–6261.

Cobb, H., 1946. Cadmium whiskers. Monthly Rev. Am. Electroplaters Soc 33 (28), 28–30.

Compton, K., Mendizza, A., Arnold, S., 1951. Filamentary growths on metal surfaces–"whiskers". Corrosion 7 (10), 327–334.

Cornelius, B., Treivish, S., Rosenthal, Y., Pecht, M., 2017. The phenomenon of tin pest: A review. Microelectronics Reliability 79, 175–192.

Deshpande, V., Sirdeshmukh, D., 1961. Thermal expansion of tetragonal tin. Acta Crystallographica 14 (4), 355–356.

Dunn, B., 1976. Whisker formation on electronic materials. Circuit World 2 (4), 32–40.

European Parliament, 2003. Directive 2002/95/EC of the European Parliament and of the Council of 27 January 2003 on the restriction of the use of certain hazardous substances in electrical and electronic equipment. Official Journal of the European Union 13, L37.

Fang, T., Osterman, M., Pecht, M., 2006. Statistical analysis of tin whisker growth. Microelectronics Reliability 46 (5-6), 846–849.

Friedrich, W., Knipping, P., Laue, M. v., 1913. Interferenzerscheinungen bei roentgenstrahlen. Annalen der Physik 346 (10), 971–988.

Fujiwara, M., Hirokawa, T., 1987. The strength of main obstacles to dislocation motion in white tin crystals. Journal of the Japan Institute of Metals and Materials 51 (9), 830–838.

Galyon, G. T., 2005. Annotated tin whisker bibliography and anthology. IEEE Transactions on Electronics Packaging Manufacturing 28 (1), 94–122.

Gaston, D., Newman, C., Hansen, G., Lebrun-Grandie, D., 2009. Moose: A parallel computational framework for coupled systems of nonlinear equations. Nuclear Engineering and Design 239 (10), 1768–1778.

Giannuzzi, L. A., Prenitzer, B. I., Kempshall, B. W., 2005. Ion-solid interactions. In: Introduction to focused ion beams. Springer, pp. 13–52.

Giannuzzi, L. A., Stevie, F. A., 1999. A review of focused ion beam milling techniques for TEM specimen preparation. Micron 30 (3), 197–204.

Hayashi, Y., Hirose, Y., Seno, Y., 2015. Polycrystal orientation mapping using scanning three-dimensional x-ray diffraction microscopy. Journal of Applied Crystallography 48 (4), 1094–1101.

Hektor, J., Marijon, J.-B., Ristinmaa, M., Hall, S. A., Hallberg, H., Iyengar, S., Micha, J.-S., Robach, O., Grennerat, F., Castelnau, O., 2018. Evidence of 3D strain gradients associated with tin whisker growth. Scripta Materialia 144, 1 – 4.

Hektor, J., Ristinmaa, M., Hallberg, H., Hall, S. A., Iyengar, S., 2016. Coupled diffusion-deformation multiphase field model for elastoplastic materials applied to the growth of Cu6Sn5. Acta Materialia 108, 98–109.

Hill, R., 1963. Elastic properties of reinforced solids: some theoretical principles. Journal of the Mechanics and Physics of Solids 11 (5), 357–372.

Jensen, D. J., Lauridsen, E., Margulies, L., Poulsen, H., Schmidt, S., Sørensen, H., Vaughan, G., 2006. X-ray microscopy in four dimensions. Materials Today 9 (1-2), 18–25.

Karma, A., Rappel, W.-J., 1998. Quantitative phase-field modeling of dendritic growth in two and three dimensions. Physical Review E 57 (4), 4323.

Kim, S. G., Kim, W. T., Suzuki, T., 1999. Phase-field model for binary alloys. Physical Review E 60 (6), 7186.

Koonce, S. E., Arnold, S., 1953. Growth of metal whiskers. Journal of Applied Physics 24 (3), 365–366.

Larson, B., Yang, W., Ice, G., Budai, J., Tischler, J., 2002. Three-dimensional X-ray structural microscopy with submicrometre resolution. Nature 415 (6874), 887–890.

Lee, B.-Z., Lee, D., 1998. Spontaneous growth mechanism of tin whiskers. Acta Materialia 46 (10), 3701–3714.

Lindborg, U., 1975. Observations on the growth of whisker crystals from zinc electroplate. Metallurgical transactions A 6 (8), 1581.

Marijon, J.-B., 2017. Caractérisation 3D de la microstructure et des déformations élastiques des polycristaux par microdiffraction Laue. Ph.D. thesis, Paris, ENSAM.

Mei, Z., Sunwoo, A., Morris, J., 1992. Analysis of low-temperature intermetallic growth in copper-tin diffusion couples. Metallurgical Transactions A 23 (3), 857–864.

Moelans, N., 2011. A quantitative and thermodynamically consistent phase-field interpolation function for multi-phase systems. Acta Materialia 59 (3), 1077–1086.

Moelans, N., Blanpain, B., Wollants, P., 2008. An introduction to phase-field modeling of microstructure evolution. Calphad 32 (2), 268–294.

NASA, 2009. Whisker failures. `https://nepp.nasa.gov/whisker/failures/index.htm`, [Online; accessed 28 August 2018].

Ohachi, T., Taniguchi, I., 1974. The growth and morphology of silver whiskers. Journal of Crystal Growth 24, 362–366.

Oudat, O., Borra, V., Georgiev, D. G., Karpov, V., 2018. The statistics of tin whisker diameters versus the underlying film grains. arXiv preprint arXiv:1806.03515.

Pei, F., Jadhav, N., Buchovecky, E., Bower, A. F., Chason, E., Liu, W., Tischler, J. Z., Ice, G. E., Xu, R., 2016. In-situ synchrotron micro-diffraction study of surface, interface, grain structure, and strain/stress evolution during Sn whisker/hillock formation. Journal of Applied Physics 119 (10), 105302.

Permann, C. J., Tonks, M. R., Fromm, B., Gaston, D. R., 2016. Order parameter re-mapping algorithm for 3D phase field model of grain growth using FEM. Computational Materials Science 115, 18–25.

Pitt, C. H., Henning, R. G., 1964. Pressure-induced growth of metal whiskers. Journal of Applied Physics 35 (2), 459–460.

Poulsen, H. F., 2004. 3DXRD–a new probe for materials science. Ph.D. thesis, Risø National Laboratory.

Poulsen, H. F., Schmidt, S., 2003. Reconstruction of grain boundaries in polycrystals by filtered back-projection of diffraction spots. Journal of applied crystallography 36 (2), 319–325.

Qin, H., Zhang, X., Zhou, M., Li, X., Mai, Y.-W., 2015. Geometry effect on mechanical performance and fracture behavior of micro-scale ball grid array structure Cu/Sn–3.0 Ag–0.5 Cu/Cu solder joints. Microelectronics Reliability 55 (8), 1214–1225.

Reyntjens, S., Puers, R., 2001. A review of focused ion beam applications in microsystem technology. Journal of micromechanics and microengineering 11 (4), 287.

Sarobol, P., Chen, W.-H., Pedigo, A. E., Su, P., Blendell, J. E., Handwerker, C. A., 2013a. Effects of local grain misorientation and β-Sn elastic anisotropy on whisker and hillock formation. Journal of Materials Research 28 (5), 747–756.

Sarobol, P., Chen, W.-H., Pedigo, A. E., Su, P., Blendell, J. E., Handwerker, C. A., 2013b. Effects of local grain misorientation and β-Sn elastic anisotropy on whisker and hillock formation–CORRIGENDUM. Journal of Materials Research 28 (05), 785–785.

Shen, C., Simmons, J., Wang, Y., 2007. Effect of elastic interaction on nucleation: Ii. implementation of strain energy of nucleus formation in the phase field method. Acta materialia 55 (4), 1457–1466.

Shishkovsky, I., Lebedev, P., 2011. 3 - Chemical and physical vapor deposition methods for nanocoatings. In: Makhlouf, A. S. H., Tiginyanu, I. (Eds.), Nanocoatings and Ultra-Thin Films. Woodhead Publishing Series in Metals and Surface Engineering. Woodhead Publishing, pp. 57 – 77.

Smetana, J., 2007. Theory of tin whisker growth:"the end game". IEEE Transactions on Electronics Packaging Manufacturing 30 (1), 11–22.

Sobiech, M., Welzel, U., Mittemeijer, E., Hügel, W., Seekamp, A., 2008. Driving force for Sn whisker growth in the system Cu–Sn. Applied Physics Letters 93 (1), 011906.

Sobiech, M., Wohlschlögel, M., Welzel, U., Mittemeijer, E., Hügel, W., Seekamp, A., Liu, W., Ice, G. E., 2009. Local, submicron, strain gradients as the cause of Sn whisker growth. Applied Physics Letters 94 (22), 221901.

Subramanian, K., Lee, J., 2006. Effects of internal stresses on the thermomechanical behavior of Sn-based solder joints. Materials Science and Engineering: A 421 (1-2), 46–56.

Susan, D., Michael, J., Grant, R. P., McKenzie, B., Yelton, W. G., 2013. Morphology and growth kinetics of straight and kinked tin whiskers. Metallurgical and Materials Transactions A 44 (3), 1485–1496.

Takaki, T., Hisakuni, Y., Hirouchi, T., Yamanaka, A., Tomita, Y., 2009. Multi-phase-field simulations for dynamic recrystallization. Computational Materials Science 45 (4), 881–888.

Teverovsky, A., 2003. Introducing a new member to the family: gold whiskers. Internal NASA Goddard Space Flight Center Memorandum, 1–6.

Ulrich, O., Biquard, X., Bleuet, P., Geaymond, O., Gergaud, P., Micha, J., Robach, O., Rieutord, F., 2011. A new white beam x-ray microdiffraction setup on the BM32 beamline at the European Synchrotron Radiation Facility. Rev. Sci. Instrum. 82 (3), 033908.

Volkert, C. A., Minor, A. M., 2007. Focused ion beam microscopy and micromachining. MRS bulletin 32 (5), 389–399.

Wikipedia contributors, 2018. Phase field models — Wikipedia, the free encyclopedia. https://en.wikipedia.org/w/index.php?title=Phase_field_models&oldid=846714701, [Online; accessed 24 August 2018].

Yang, F., Li, J., 2006. Deformation behavior of tin and some tin alloys. In: Lead-Free Electronic Solders. Springer, pp. 191–210.

Zhang, J., Poulsen, S. O., Gibbs, J. W., Voorhees, P. W., Poulsen, H. F., 2017. Determining material parameters using phase-field simulations and experiments. Acta Materialia 129, 229–238.

Zhou, B., Bieler, T. R., Lee, T.-K., Liu, K.-C., 2009. Methodology for analyzing slip behavior in ball grid array lead-free solder joints after simple shear. Journal of electronic materials 38 (12), 2702.